



1    **Spatial and morphometric analysis of a comprehensive dataset of**  
2    **loess sinkholes from a small basin in the Chinese Loess Plateau**

3                    Sheng Hu<sup>1,2</sup>, Francisco Gutiérrez<sup>3</sup>, Fanyu Zhang<sup>4</sup>, Sisi Li<sup>1,5</sup>, Ninglian Wang<sup>1,2</sup>,  
4                    Xi-an Li<sup>6</sup>, Xingang Wang<sup>7</sup>, Jinhui Sun<sup>1</sup>, Songbai Wu<sup>1,2</sup>

5                   <sup>1</sup> Shaanxi Key Laboratory of Earth Surface System and Environmental Carrying  
6                    Capacity, College of Urban and Environmental Sciences, Northwest University, Xi'an  
7                    710127, China

8                   <sup>2</sup> Institute of Earth Surface System and Hazards, Northwest University, Xi'an 710127,  
9                    China

10                   <sup>3</sup> Departamento de Ciencias de la Tierra, Universidad de Zaragoza, C/ Pedro Cerbuna 12,  
11                    50009 Zaragoza, Spain

12                   <sup>4</sup> MOE Key Laboratory of Mechanics on Disaster and Environment in Western China,  
13                    Department of Geological Engineering, Lanzhou University, Lanzhou 730000, China

14                   <sup>5</sup> School of Information Science and Technology, Northwest University, Xi'an 710127,  
15                    China

16                   <sup>6</sup> School of Geological Engineering and Geomatics, Chang'an University, Xi'an 710054,  
17                    China

18                   <sup>7</sup> State Key Laboratory of Continental Dynamics, Department of Geology, Northwest  
19                    University, Xi'an 710069, China

20

21                   **Correspondence:** Fanyu Zhang (zhangfy@lzu.edu.cn)

22



23 **Abstract.** From the perspective of the world, the basic mapping and investigation of the loess  
24 sinkhole is far less extensive and in-depth than that of the karst sinkhole survey. To some extent,  
25 this hinders people's understanding of the morphological characteristics, development rules,  
26 and formation mechanisms of the loess sinkholes. Chinese Loess Plateau (CLP) has the most  
27 typical loess landform in the world, and tens of thousands of loess sinkholes have developed.  
28 However, due to the lack of high-precision and high-resolution survey data, the identification,  
29 characterization, and quantification of sinkholes in the Loess Plateau are basically blank, which  
30 seriously hinders the in-depth study of loess sinkholes. We investigated a typical watershed on  
31 the Chinese Loess Plateau using photogrammetry, airborne laser scanning, and handheld laser  
32 scanner. Based on previous studies, this paper proposes indices and methods for the  
33 morphological quantification of loess sinkholes and constructs the first dataset of loess sinkhole  
34 morphology containing 1194 records at the basin scale. On this basis, we completed the spatial  
35 mapping of loess sinkholes, analysis of distribution patterns, morphological analysis, size-  
36 frequency analysis, fitting analysis of different parameters, estimation of subsurface soil erosion,  
37 in-depth investigation of typical sinkholes, and quantification of the contributions of different  
38 factors to sinkhole development. These efforts provide rich information for a deeper  
39 understanding of the morphological characteristics and causes of loess sinkholes and offer data  
40 support for comparative studies with sinkholes in other regions. More critically, we  
41 preliminarily assessed that the subsurface soil erosion triggered by sinkholes in the study area  
42 amounts to as high as 345,000 metric tons. This finding makes it increasingly clear that loess  
43 sinkholes are not only a geological disaster process but also a serious soil loss process,



44 highlighting their undeniable significance in regional soil erosion studies and laying a solid  
45 foundation for subsequent research and disaster prevention efforts. Moreover, we believe that  
46 the integration of airborne laser scanning and handheld laser scanning may represent a new  
47 trend in the detailed investigation of sinkholes in the future. The dataset is available from  
48 Zenodo platform (<https://doi.org/10.5281/zenodo.14000267>).

## 49 **1 Introduction**

50 It is widely recognized that soil erosion constitutes a global environmental problem with  
51 significant societal and economic implications (Morgan, 2005; Poesen, 2018; Llena et al., 2024).  
52 When the term ‘soil erosion’ is used, most people picture surface processes such as sheet, rill,  
53 gully, or gravity erosion. However, subsurface mechanical erosion related to soil piping and the  
54 associated surface collapse is widely overlooked (Bernatek-Jakiel and Poesen, 2018). The vast  
55 international literature on soil erosion reveals an evident knowledge gap regarding soil piping  
56 research. Soil piping refers to the formation of shallow conduits in soils and weakly  
57 consolidated sediments by seepage, pipe flow, and mass movements (e.g., wall and roof  
58 collapse) (Bernatek-Jakiel and Poesen, 2018). Soil pipes, due to their hidden nature and  
59 complex patterns, are detected only once their collapse reaches the surface to form a sinkhole  
60 (Donnelly, 2008; Bernatek, 2015; Bernatek-Jakiel et al., 2017). Ground instability associated  
61 with sinkhole development poses threats to agriculture, transportation infrastructure, water  
62 storage facilities, oil and gas pipelines, buildings, and other human assets and activities (Gibbs,  
63 1945; Gutiérrez et al., 2003, 2014; Richards and Reddy, 2007; Peng et al., 2018; Hu et al., 2020).  
64 Piping sinkholes cause soil erosion and can induce or favor hazardous processes such as ground



65 collapse, landsliding, debris flows, or gullying (Peng et al., 2018; Li et al., 2020; Hu et al., 2022;  
66 Wang et al., 2024). Therefore, gaining insight into the factors controlling piping-related  
67 sinkholes, their morphometry and spatial distribution patterns is of prime scientific and practical  
68 importance (Hofierka et al., 2018; Bernatek-Jakiel et al., 2019).

69 The identification of sinkholes and the production of comprehensive sinkhole inventories  
70 are a fundamental and challenging task. In recent decades, several countries have conducted  
71 extensive research on karst and piping sinkholes and developed national or regional  
72 geodatabases (Gao et al., 2002, 2005; Farrant and Cooper, 2008; Rajabi, 2018; Vennari and  
73 Parise, 2022; Hu et al., 2024). Traditional sinkhole mapping primarily relies on topographic  
74 maps, digital elevation models (DEM), historical aerial photography, or satellite imagery  
75 (Panno et al., 1997; Panno and Luman, 2013; De Carvalho Júnior et al., 2014; Vajedian and  
76 Motagh, 2019; Gökkaya et al., 2021). However, data acquired through conventional methods  
77 are often hampered by poor spatial resolution, making them inadequate for the comprehensive  
78 and accurate mapping and morphometric characterization of soil sinkholes, which are usually  
79 small. Consequently, researchers have started to use unmanned aircraft systems (UAS)  
80 equipped with optical lenses, LiDAR sensors, and thermal cameras to investigate piping  
81 sinkholes (Lee et al., 2016; Wu et al., 2016; Hofierka et al., 2018; Hu et al., 2020; Li et al.,  
82 2024). UAS technology can capture imagery and topographic data with high resolution and  
83 accuracy, and may even allow for filtering vegetation in the case of LiDAR data. Despite the  
84 variety of techniques and approaches currently available, each still carries inherent limitations  
85 or shortcomings (Bernatek-Jakiel and Poesen, 2018). For instance, although UAS-based

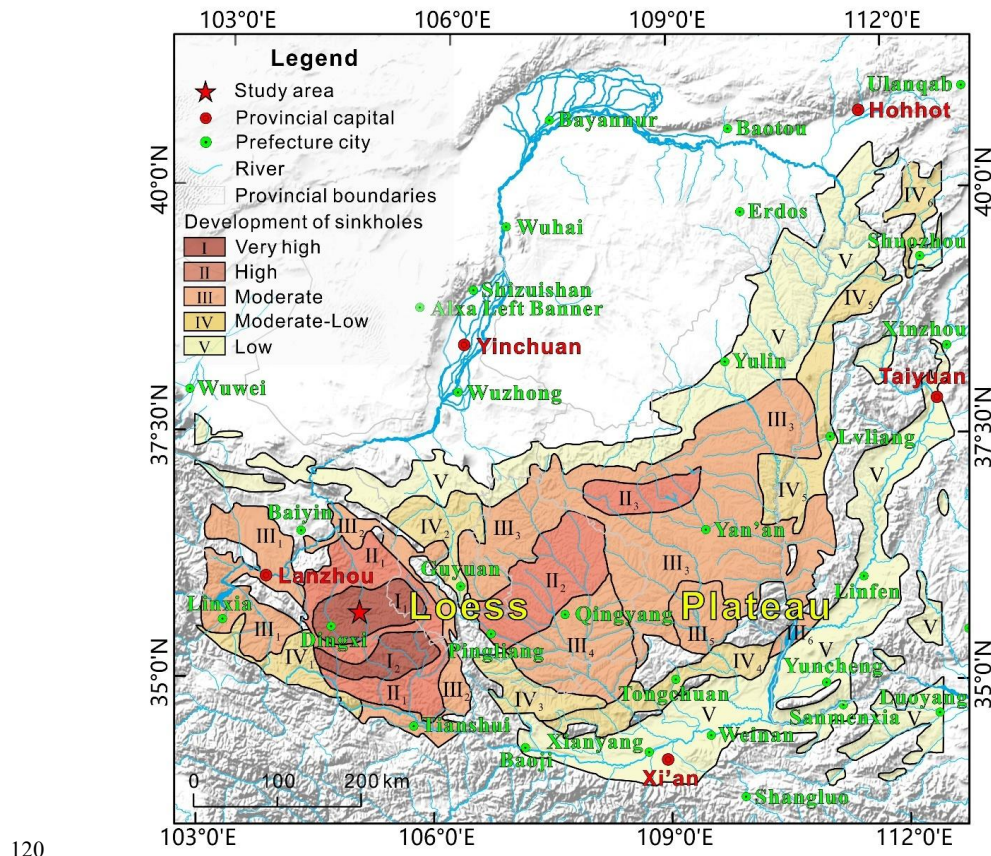


86 photogrammetry can yield high-resolution topographic models, those models do not allow the  
87 reliable measurement of 3D morphometric parameters of piping sinkholes, such as depth or  
88 volume (Li et al., 2024). Airborne LiDAR, while capable of partly penetrating vegetation to  
89 reveal the underlying ground surface, typically employs orthogonal scanning, missing zones  
90 along the vertical walls of collapsed pipes, and thus failing to capture the complete inner  
91 morphology of the sinkholes (Jiang et al., 2024). The aforementioned mapping technologies  
92 and methods are suitable for regional sinkhole surveys, but are not suitable for characterizing  
93 the internal morphology of individual sinkholes. In recent years, handheld laser scanners based  
94 on simultaneous localization and mapping (SLAM) technology have been developed and  
95 successfully applied to forest surveys, archaeological studies, tunnel, and sinkhole  
96 investigations (Jones and Beck, 2017; Konsolaki et al., 2020; Mokroš et al., 2021; Yuan et al.,  
97 2022; Hu et al., 2024; Jiang et al., 2024). When conducting non-destructive identification and  
98 characterization of soil pipes and the associated sinkholes, it is essential to select the most  
99 suitable investigation technique or to combine several complementary methods considering  
100 factors such as the characteristics of the target features and the survey area (Bernatek-Jakiel and  
101 Kondracka, 2016; Borah et al., 2022).

102 A recent review on soil piping (Bernatek-Jakiel and Poesen, 2018) provides a global  
103 synthesis of current knowledge and delineates directions for future research. By collating data  
104 from 230 documented piping sites worldwide, the authors produced the first global map of soil-  
105 piping investigations, demonstrating that piping erosion occurs across all climate zones and  
106 most soil types. Regrettably, the review reveals a striking paucity of research on soil pipes in



107 the Chinese Loess Plateau (CLP), with only two documented study sites. It is widely recognized  
108 that the CLP, covering  $64 \times 10^4 \text{ km}^2$ , hosts the world's most representative loess accumulation.  
109 Due to the relatively high permeability, collapsibility, and wetness of loess deposits, together  
110 with its porous and jointed structure, pipes and sinkholes can easily form under the presence of  
111 water (Li et al., 2010; Geng et al., 2023). In recent years, some scholars in China have identified  
112 loess sinkholes as a specific geological hazard and have called for increased focus and research  
113 on this process with growing economic implications (Li et al., 2010, 2020; Peng et al., 2018).  
114 The intensity map of sinkhole development in the Chinese Loess Plateau (Fig. 1) indicates that  
115 the west region exhibits a higher intensity of sinkhole development compared to the east,  
116 particularly in the Dingxi and Huining areas, where sinkhole densities typically reach 243 and  
117 265 sinkholes per  $\text{km}^2$ , respectively (polygon I<sub>1</sub> in Figure 1) (Peng et al., 2018; Hu et al., 2020).  
118 Notably, no regional morphometric datasets of piping sinkholes have yet been published,  
119 limiting our understanding of their morphological characteristics and developmental patterns.



121 **Figure 1.** Map showing the degree of piping-related sinkhole development in the Chinese  
122 Loess Plateau, classified into five categories (Peng et al., 2018; Hu et al., 2020). The star  
123 indicates the location of the study area within a region with very high degree of sinkhole  
124 development.

125 In view of the above, the principal objectives of this study include: (1) to conduct a  
126 comprehensive and high-resolution survey of loess sinkholes in a representative basin of the  
127 CLP by integrating UAS photogrammetry, airborne LiDAR, and a SLAM-based handheld laser  
128 scanner (HLS); (2) to characterize the morphometric features of the sinkholes and produce an  
129 open-access database comprising 1194 sinkhole records, complemented with data on multiple



130 attributes; (3) to analyze the spatial distribution patterns of the sinkholes and their relationships  
131 with other landforms in order to gain insight into the main controlling factors; (4) to carry out  
132 an in-situ investigation inside a typical sinkhole using the HLS, evaluating the potential and  
133 advantages of SLAM technology for full sinkhole characterization. Through these efforts, we  
134 aim to partially fill the current knowledge gap on loess sinkholes in the CLP and identify  
135 suitable surveying approaches. This will make available to the global soil-piping community  
136 with a unique case-study dataset and will provide a scientific basis for assessing and managing  
137 sinkhole risk in the region. The presented results reveal the strikingly large subsurface erosion  
138 volume attributable to piping erosion, underscoring that soil-piping research merits intensified  
139 attention, rather than continued neglect.

140 **2 Study area**

141 The study area is a small leaf-shaped watershed drained by the N-flowing Sunjiacha stream.  
142 It is located in the southwestern sector of the Loess Plateau of China, approximately 5 km east  
143 of Huining city (Figs. 2a-c). The drainage basin is approximately 2960 m long, 1280 m wide,  
144 covers about 2.4 km<sup>2</sup>, and displays sparse grassland vegetation. The elevation ranges from 2070  
145 m a.s.l. (highest point of the divide) to 1724 m a.s.l. (outlet), yielding a local relief of 346 m.  
146 The region is characterized by a semi-arid temperate monsoon climate, with a mean annual  
147 precipitation of 370 mm. Great part of the rainfall occurs between May and September and  
148 frequent severe rainfall events can account for up to 96% of the monthly precipitation (Hu et  
149 al., 2020). Sunjiacha stream is an ephemeral channel that carries water flow after storms or  
150 rainy periods. Great part of the slopes in the basin, with the exception of some sectors in the



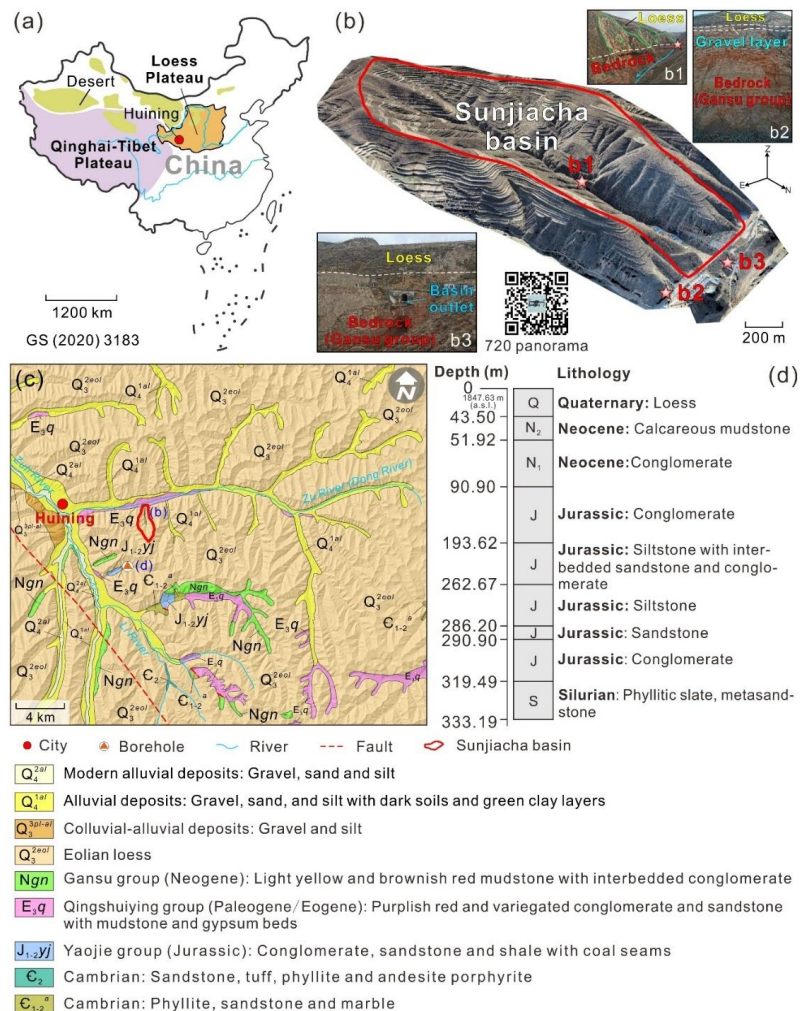
151 lower part, have been transformed into a terraced landscape on loess deposits for cultivation  
152 and to prevent soil erosion (Fig. 2b).

153 Form the geological perspective, the investigated zone is located in the Longxi Basin. Its  
154 development began during the Yanshan orogeny (ca. 205~66 Ma), expanded further during the  
155 Himalayan orogeny (ca. 50 Ma to present), and finally took shape as the Longxi graben basin  
156 by the late Neogene. The basement of the basin is composed of Proterozoic metamorphic rocks,  
157 Paleozoic volcano-sedimentary rocks, Caledonian intrusive rocks and Mesozoic-Cenozoic  
158 sedimentary successions. Since the end of Neogene to Quaternary, the Longxi Basin has been  
159 uplifted along with the Qinghai-Tibet Plateau and its surrounding mountains (Niu, 2023). The  
160 tectonic uplift in the Quaternary has been accompanied by (Figs. 2b, c): (1) downcutting of the  
161 drainage network into the Neogene sediments of the Gansu group; and (2) accumulation of  
162 loess and terraces over the relatively flat Gansu group red beds, forming a thick loess-paleosoil  
163 succession. The 1:200,000 scale regional geological map indicates that most slopes in the area  
164 are underlain by the Q<sub>3</sub> aeolian loess (Malan loess), while Q<sub>4</sub> alluvial and colluvial deposits,  
165 largely derived from the former, primarily occur in the valley floors (Fig. 2c). Fig. 2d shows a  
166 simplified log of the 333 m deep Huining #11 borehole drilled 2.6 km S of the Sunjiacha basin  
167 by the China Geological Survey in 1972, indicating a Quaternary loess 43.5 m thick. In the  
168 1960s, Liu (1964, 1965) observed a gradual NW-to-SE grain-size decrease in the loess in the  
169 Loess Plateau, and divided it into three zones: sand loess, typical loess, and clayey loess. This  
170 spatial pattern is attributed to factors such as the distance from the source area and the  
171 southeastward weakening of winds in winter (Yang and Ding, 2017). Previous studies have



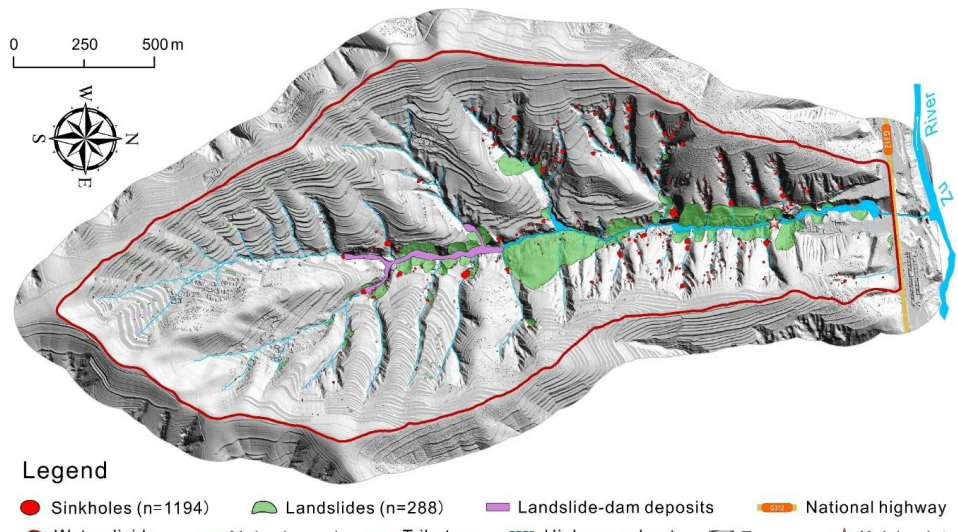
172 shown that the Huining loess has both dust from inland desert areas and detritus generated  
173 during the Pleistocene glaciations on the Qinghai-Tibet Plateau (Peng, 2014). Because Huining  
174 is close to both source regions, relatively coarse sand and silt particles were deposited here by  
175 the northwesterly winds. Thus, the large pore size characteristic of the Q<sub>3</sub> Malan loess is  
176 particularly pronounced in this area. The Q<sub>3</sub> Malan loess is a light grey-yellow silt-dominated  
177 deposit with relatively uniform particle distribution, loose granular texture and blocky  
178 morphology. The grain size of the loess-paleosol sequence at Duanxian site (S0~L29; 62 km  
179 north of our study area) studied by Niu (2023) is generally coarse, with a median particle size  
180 ranging from 12 to 38.8  $\mu\text{m}$  (silt size range: 2~50  $\mu\text{m}$ ). Particles >32  $\mu\text{m}$  and >63  $\mu\text{m}$  represent  
181 around 60% and 25% of the silt-dominated deposit, respectively (Niu, 2023).

182 The thickness of the Q<sub>3</sub> Malan loess is highly variable, ranging from several meters to tens  
183 of meters. Under the presence of infiltration water, the Q<sub>3</sub> Malan loess, commonly affected by  
184 vertical joints, is highly susceptible to hydrocompaction and piping, leading to the formation of  
185 unique loess sinkhole landscapes. In fact, this area is widely recognized as having the highest  
186 density of loess sinkholes in the vast Loess Plateau, covering 6370 km<sup>2</sup> (2.33% of the loess  
187 accumulation in China) (Fig. 1). Average density of sinkholes in our study area is 498  
188 sinkholes/km<sup>2</sup>. The investigated drainage basin, characterized by a dendritic gully network and  
189 terraced slopes, displays a large number of loess-related ground instability features, including  
190 1194 loess collapse sinkholes and 288 landslides (Fig. 3). The latter include slope movements  
191 with deep and shallow sliding surfaces, typically induced by fluvial undercutting, artificial  
192 excavations, and severe rainfall events.



193

194 **Figure 2.** Geographic and geological setting of the Sunjiacha drainage basin within the Loess  
 195 Plateau. (a) Location in the SW Loess Plateau in China. (b) 3D model of the Sunjiacha basin  
 196 generated by Structure from Motion Photogrammetry with UAS images. The QR code gives  
 197 access to an online panorama of the study area generated with drone images. (c) 1:200,000  
 198 scale regional geological map (data source: <http://dcc.ngac.org.cn/>); (d) Stratigraphic log of  
 199 the Huining #11 borehole drilled for coal exploration 2.6 km south of the study area (see  
 200 location in c) (data source: <http://zk.cgsi.cn/>).



201  
202 **Figure 3.** Geomorphological map showing the distribution of loess sinkholes, landslides and  
203 deposits accumulated upstream of a landslide dam in the Sunjiacha basin.  
204

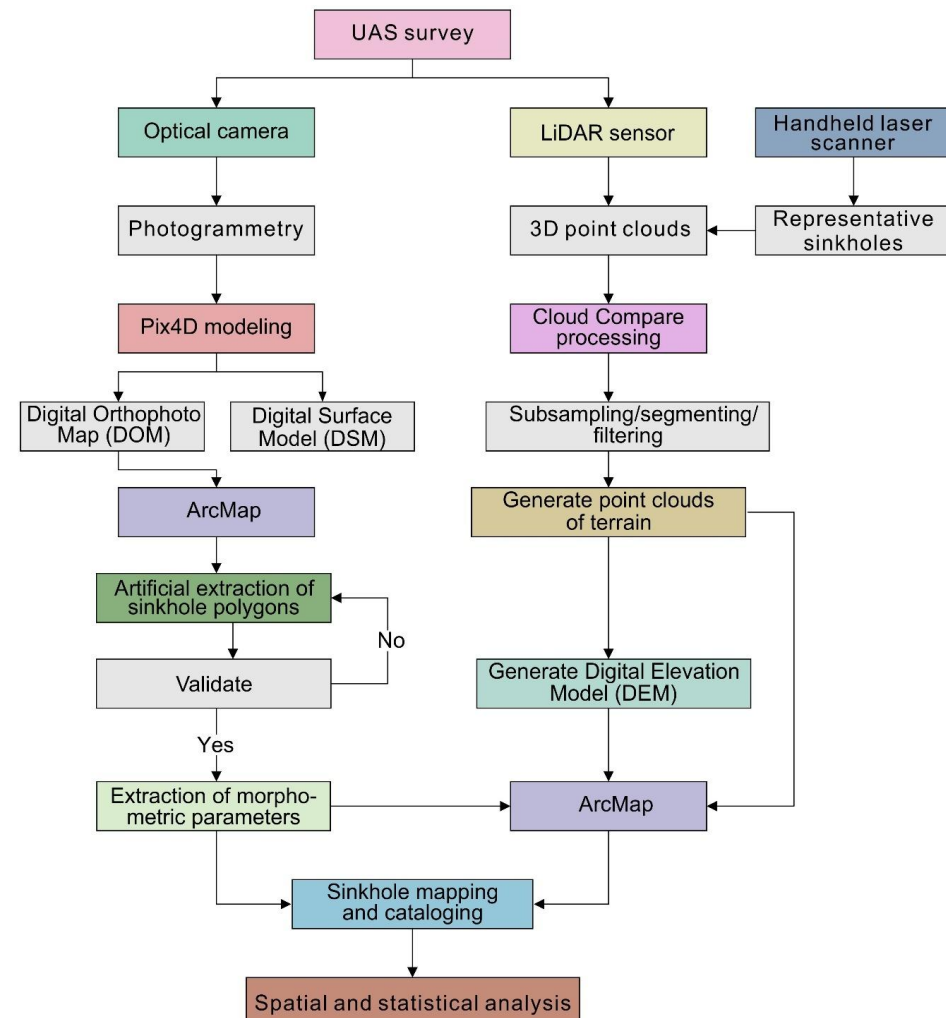
### 3 Methods

#### 3.1 Technical procedure

206 The flow diagram in [Figure 4](#) outlines the data acquisition and analysis approach followed  
207 in this investigation, comprising several steps. Initially, we conducted surveys using an  
208 unmanned aircraft system (UAS) equipped with optical cameras and LiDAR sensors, as well  
209 as utilizing a handheld laser scanner (HLS). Subsequently, the data collected in the surveys  
210 allowed the generation of a Digital Orthophoto Map (DOM), a bare-surface Digital Surface  
211 Model (DSM), a Digital Elevation Model (DEM), and 3D terrain point clouds. The drone  
212 imagery was processed using the Structure from Motion Photogrammetry software Pix4D  
213 Mapper (<https://www.pix4d.com/>), while the open-source Cloud Compare software  
214 (<http://www.cloudcompare.org/>) was utilized for analyzing the point clouds. ArcMap 10.5 was



215 used to manually map the sinkholes and extract planimetric and three-dimensional  
216 morphometric parameters by using the DOM, DEM and relief maps. This allowed the  
217 construction of a cartographic sinkhole inventory including a number of categorical and  
218 numerical attributes for the morphometric and statistical analysis of the sinkholes. 3D data of  
219 the loess sinkholes such as elevation and depth were extracted from noise-filtered terrain point  
220 clouds acquired with airborne LiDAR, rather than directly from the UAS-derived DSM,  
221 significantly enhancing the accuracy of the parameters.



222

223 **Figure 4.** Flow chart illustrating the data collection, processing and analysis approaches used  
224 in this study.

225 **3.2 Field investigations**

226 **3.2.1 UAS survey**

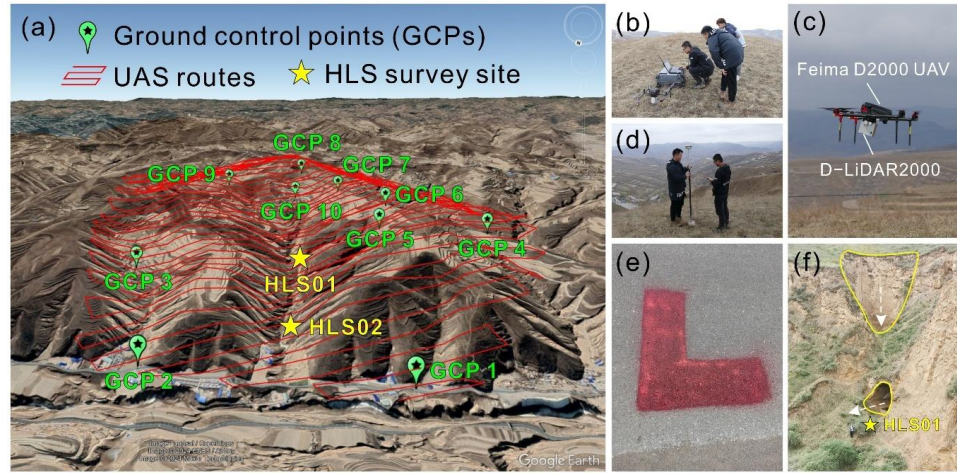
227 On April 9, 2021, we engaged the professional company Feima Robotics to conduct a  
228 detailed survey of the research area using a D2000 UAS (Figs. 5a-e). We executed two flight



229 missions at a height of 200 m utilizing the D-Lidar 2000 LiDAR sensor and the D-CAM2000  
230 optical camera mounted on the drone. Images were taken with longitudinal and lateral overlaps  
231 of 70% and 60%, respectively. Point clouds were taken with lateral overlap of 40%. A total of  
232 11 ground control points (GCPs) were distributed across the area and measured with a DGPS.  
233 Detailed specifications of the UAS and its sensors are available at  
234 <http://www.feimarobotics.com/zhcn/productDetailD2000>. The D-Lidar 2000 module employs  
235 three-echo technology, ensuring effective penetration through vegetation to obtain more  
236 accurate bare-ground data. After completing the field survey, we pre-processed the collected  
237 data with the UAV Manager software to produce a 3 cm resolution Digital Orthophoto Map  
238 (DOM) and a Digital Surface Model (DSM), along with raw point cloud data (40 GB; average  
239 density of 192 points/m<sup>2</sup>). The modeling report from UAV Manager indicated that the average  
240 RMSE (root-mean-square error) for the 11 ground control points (GCPs) was 0.0137 m, with  
241 RMSEs of 0.012 m, 0.014 m and 0.015 m for the X, Y and Z coordinates, respectively. An  
242 elevation accuracy assessment of 19 laser point cloud validation points measured with the  
243 DGPS revealed an average RMSE of 0.029 m, with a maximum error of 0.058 m.



244



245 **Figure 5.** Surveying of the study area with an UAS (Li et al., 2024)  
246 and a handheld laser scanner: (a) Terrain model of the study area draped by a Google Earth image. Red lines  
247 indicate the route of the UAS. Green paddle icons show the distribution of ground control  
248 points (GCPs) used to improve the accuracy of the UAS models. Yellow stars indicate the  
249 location of the handheld laser scanner surveys. (b-e) Unmanned aerial system field operations  
250 with the control unit (c) and the drone (d), combined with GCPs (e) measured with a DGPS  
251 (d); (f) Using the GeoSLAM (ZEB Horizon) handheld laser scanner to scan the interior of a  
252 sinkhole in a steep slope with an opening at the bottom.

253 **3.2.2 Handheld laser scanner survey**

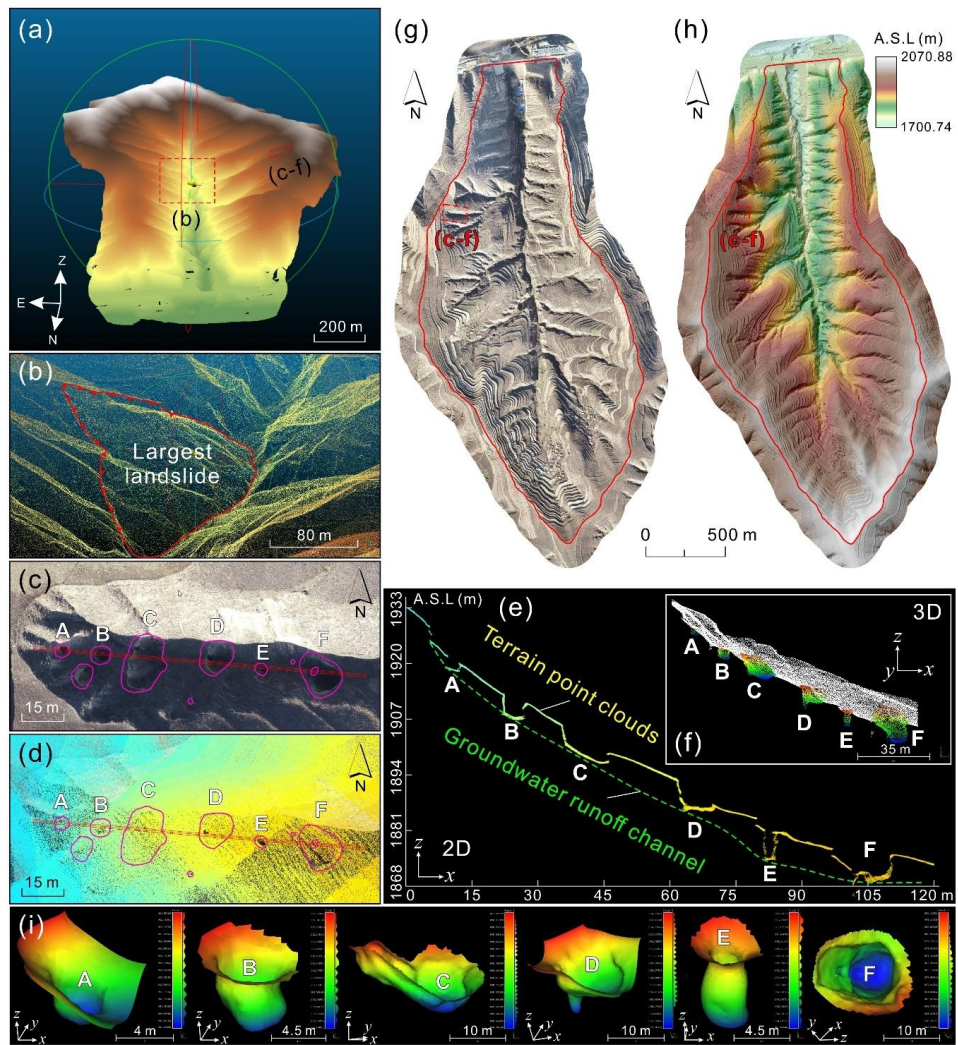
254 We used a GeoSLAM ZEB Horizon handheld LiDAR scanner (<https://geoslam.com/>) with  
255 a range of 100 m to carry out high-resolution scans of thirteen representative sinkholes (1  
256 sinkhole in HLS01 site; 12 sinkholes in HLS02 site; see location in [Figures 5a, f](#)). This device  
257 utilizes SLAM (Simultaneous Localization and Mapping) technology, which can record point  
258 cloud data of the terrain or objects in real-time obtaining accurate geographic coordinates. It  
259 weighs 1.45 kg, and records 300,000 points per second with a measurement error of 6 mm to 3  
260 cm. After the field survey, we pre-processed and post-processed the point cloud data using



261 GeoSLAM Draw and Cloud Compare software and subsequently we obtained noise-filtered  
262 terrain point clouds and DEMs of the representative sinkholes.

263 **3.2.3 Surveying and mapping**

264 [Figure 6](#) illustrates some of the products derived from the UAS survey. We filtered the raw  
265 point clouds using the Cloth Simulation Filter (CSF) developed by [Zhang et al. \(2016\)](#) in Cloud  
266 Compare. The main parameter settings were: General parameter setting – check Steep slope  
267 and Slop processing options; Advanced parameter setting – Cloth resolution 0.5 m, Maximum  
268 iterations 999, Classification threshold 0.1 m. [Figure 6a](#) shows the terrain point cloud processed  
269 in Cloud Compare with above-surface noise filtered out (buildings, people, vehicles, vegetation,  
270 towers, and power lines). [Figures 6b-f](#) show enlarged views of the dashed boxes indicated in  
271 [Figures 6a, g-h](#). [Figure 6b](#) illustrates the largest landslide of the study area. [Figures 6c and 6d](#)  
272 depict an orthoimage and a terrain point cloud of a gully with a string of sinkholes related to a  
273 subsurface conduit created by internal erosion. [Figures 6e and 6f](#) display the 2D profile of the  
274 terrain point cloud and an excerpt of the 3D point cloud of a gully with numerous sinkholes,  
275 respectively. [Figure 6g](#) shows the 6.87 cm resolution Digital Orthophoto Map (DOM) derived  
276 from the drone images. [Figure 6h](#) presents the 0.5 m resolution Digital Elevation Model (DEM)  
277 generated from the terrain point cloud data in [Figure 6a](#). [Figure 6i](#) depicts the 3D models  
278 generated by Poisson Surface Reconstruction in Cloud Compare, based on LiDAR point-cloud  
279 data from six sinkholes. These spatial data provide the basis for mapping and cataloging  
280 sinkholes, identifying sediment-discharge holes, and extracting morphometric parameters.



281

282

Figure 6. UAS survey results: (a) Bare-surface point cloud of the study area after filtering above-surface objects; (b-f) Partial enlargements of (a); (b) Largest landslide of the study area; (c-e) Orthoimage, point cloud, and a point-cloud section of a row of loess sinkholes (purple line in d) in a collapsed gully, respectively; (f) 3D perspective of (d); (g) Digital orthophoto map (DOM) generated from images captured by the UAS survey; (h) Digital elevation model (DEM) generated from bare-surface point clouds; (i) Poisson surface reconstruction of sinkholes A-F in d.

283

284

285

286

287

288



289 **3.3 Basic morphometric parameters and extraction methods**

290 Based on a literature review on studies about loess sinkholes and karst dolines worldwide,  
291 we selected a number of morphometric parameters for the geometrical characterization of the  
292 loess sinkholes (e.g., [Day, 1983](#); [Liu and Wang, 2008](#); [De Waele and Gutiérrez, 2022](#) and  
293 references therein). [Table 1](#) presents the selected some parameters, their definition and the  
294 approach used for their automatic computation. Key morphological parameters and their  
295 interpretations are illustrated in [Figure 7](#).



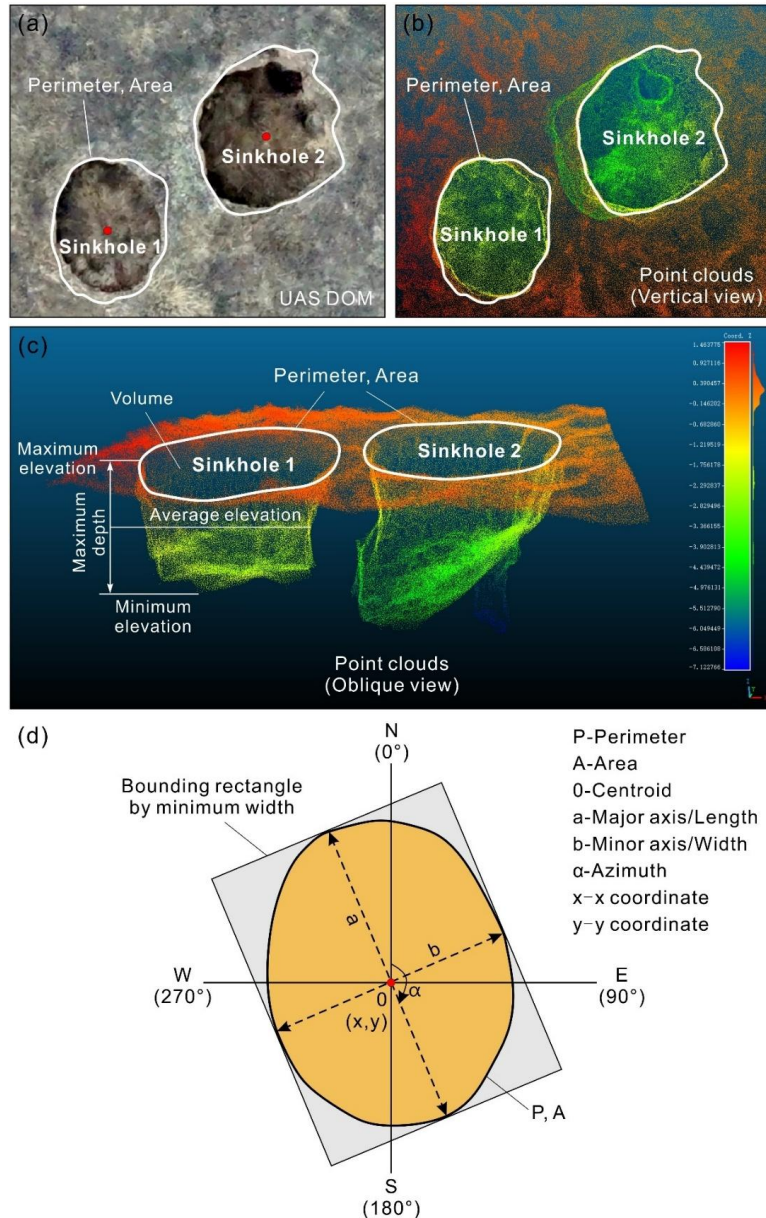
296

**Table 1** Index, definition and computing method of morphology of loess sinkholes.

Parameter	Unit	Computing method	Explanation	Reference
Coordinates	°	Calculate geometry in ArcMap attribute table	X, Y coordinates of the centroid of the sinkhole polygon	
Length ( $L$ )	m	Length of the fitted minimum bounding rectangle	Length of the major axis, given by the planimetric distance between the antipodal points of the perimeter	Kobal et al, 2015; Wu et al, 2016
Width ( $W$ )	m	Width of the fitted minimum bounding rectangle	Width perpendicular to major axis, given by the width of the fitted minimum bounding rectangle	Kobal et al, 2015; Wu et al, 2016
Azimuth ( $Azi$ )	°	ArcMap Minimum Bounding Geometry tool	Clockwise angle between the North and the major axis	Bruno et al, 2008; Kobal et al, 2015; Öztürk et al, 2018
Maximum elevation ( $E_{max}$ )	m	Extracted from point cloud data	Maximum elevation of the sinkhole perimeter	
Minimum elevation ( $E_{min}$ )	m	Statistics by Area tool in ArcMap	Minimum elevation at the sinkhole bottom	
Average elevation ( $E_{ave}$ )	m	Extracted from point cloud data	Average elevation of the 3D points that define the sinkhole depression	
Maximum depth ( $D_{max}$ )	m	Extracted from point cloud data	Maximum elevation minus minimum elevation	De Waele and Gutiérrez, 2022; Sevil and Gutiérrez, 2023
Perimeter ( $P$ )	m	Calculate geometry in ArcMap attribute table	Planimetric length of the mapped edge of the sinkhole	Liu and Wang, 2008
Area ( $A$ )	$m^2$	Calculate geometry in ArcMap attribute table	Planimetric area enclosed by the perimeter	Liu and Wang, 2008
Volume ( $V$ )	$m^3$	$V=A \times D_{max}$	Volume of the 3D space corresponding to the sinkhole depression	Gökkaya et al., 2021; De Waele and Gutiérrez, 2022



Elongation ratio ( <i>ER</i> )	$ER=L/W$ or $ER=a/b$ , where $L$ (or $a$ ) and $W$ (or $b$ ) are the major and minor axes (length and width) of the sinkhole, respectively	Length to width ratio	Day, 1983; Basso et al., 2013; Zumpano et al., 2019
Circularity index ( <i>CLI</i> )	$CLI = 4\pi A/P^2$	Ratio between the area of the sinkhole and the area of a theoretical sinkhole having a circumference equal to the perimeter of the actual sinkhole. The lower the value below 1, the further to a perfect circular shape	De Carvalho Júnior et al., 2014
Compactness index ( <i>COI</i> )	$COI = A/Ac$ , where $Ac$ is the area of the smallest circle circumscribing the sinkhole perimeter	Quantifies how much the shape of the sinkhole perimeter is close to a circle. The lower the value below 1, the more complex the sinkhole perimeter	Cole, 1964; Kim and Anderson, 1984; Li et al., 2013; Zhu and Pierskalla, 2016
Length to Depth ratio ( <i>LDr</i> )	$LDr=L/D_{max}$	Ratio between sinkhole length and depth	Day, 1983



298

299 **Figure 7.** Diagrams showing the key morphometric parameters of the loess sinkholes: (a)  
300 Images of sinkholes; (b) Point clouds of sinkholes (located at HLS 02 in [Figure 5a](#)) in vertical  
301 view; (c) Point clouds of sinkholes in oblique view; (d) Diagram of key morphometric  
302 parameters of sinkholes.



303 **4 Results**

304 **4.1 Sinkhole mapping and inventorying**

305 Given the utmost high-resolution of the data used for mapping, the inventory can be  
306 considered as complete, even including small decimeter-scale holes. This information furnished  
307 a database of 1194 loess sinkholes in the study area, including multiple attributes ([Table 1](#) and  
308 [Data availability](#)): topographic (coordinates, azimuth, maximum, minimum and average  
309 elevation); morphometric (length, width, depth, perimeter, area, volume, geometrical indexes);  
310 and geomorphic (soil loss). The inventory also differentiates 1162 single sinkholes, and 32  
311 compound sinkholes resulting from the aggregation of two or more adjacent sinkholes. This  
312 complete database serves as the basis for the morphometric-statistical analysis presented in this  
313 work. For the detailed cataloging and the statistical parameters of these sinkholes, please refer  
314 to [Table 2](#) and [Data availability](#). Additionally, 9 thematic maps were generated with some  
315 parameters (length, maximum depth, perimeter, area, volume, elongation ratio, circularity index,  
316 compactness index, length to depth ratio) to explore spatial patterns of different value ranges.  
317 [Table 2](#) presents the main statistics of the sinkholes separated into three categories: all, single  
318 and compound.



319

**Table 2** Main statistics of different types of sinkholes.

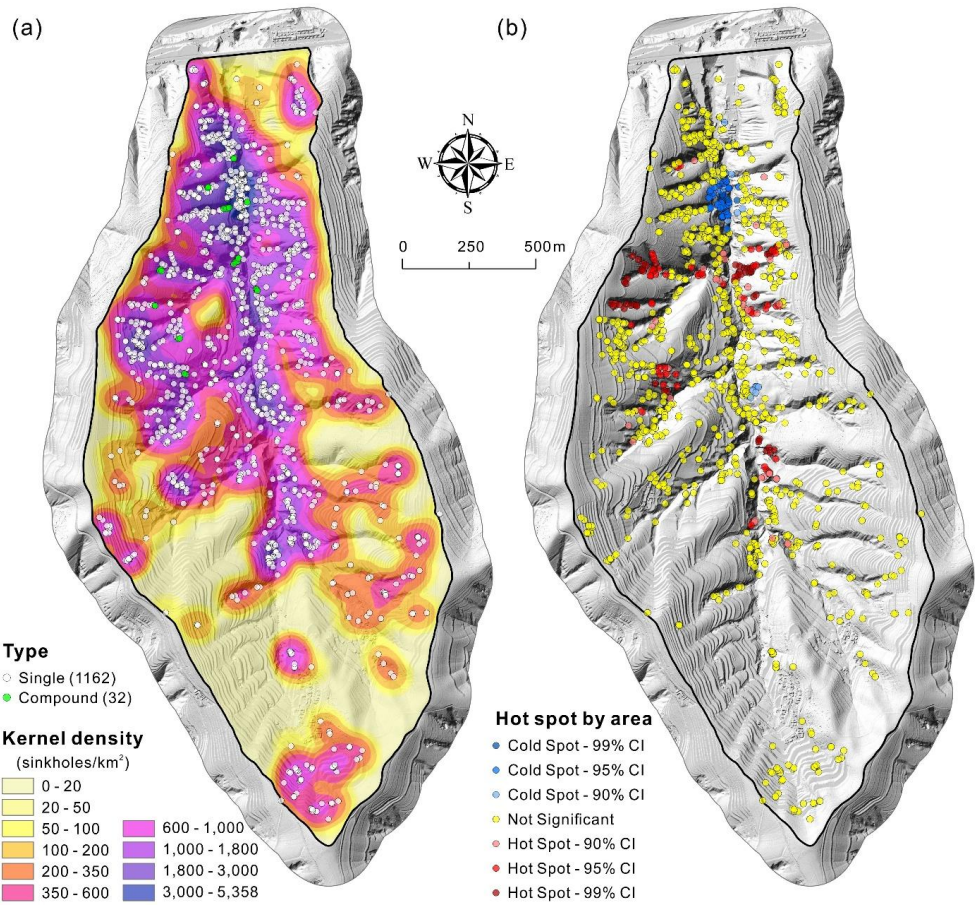
Statistical indicators	All sinkholes (1194)	Single sinkholes (1162)	Compound sinkholes (32)
<b>Length (m)</b>			
Range	0.19~35.11	0.19~35.11	0.88~33.9
Mean	3.75	3.65	7.37
Median	2.28	2.26	3.69
<b>Depth (m)</b>			
Range	0.42~29.60	0.42~29.60	2.05~18.50
Mean	6.55	6.48	8.36
Median	5.30	5.214	7.76
<b>Perimeter (m)</b>			
Range	0.60~104.14	0.60~98.92	2.67~104.14
Mean	10.75	10.45	21.51
Median	6.43	6.40	10.47
<b>Area (m<sup>2</sup>)</b>			
Range	0.03~662.18	0.03~662.18	0.50~635.75
Mean	17.75	16.42	66.19
Median	2.94	2.93	7.97
<b>Volume (m<sup>3</sup>)</b>			
Range	0.21~19601.27	0.21~19601.27	2.66~8405.93
Mean	334.75	310.79	1002.98
Median	42.78	42.10	81.28
<b>Elongation ratio</b>			
Range	1~4.55	1~4.55	1.04~1.98
Mean	1.37	1.37	1.31
Median	1.30	1.30	1.28
<b>Circularity index</b>			
Range	0.33~0.98	0.33~0.98	0.74~0.96
Mean	0.89	0.89	0.88
Median	0.92	0.92	0.90
<b>Compactness index</b>			
Range	0.45~0.88	0.45~0.88	0.70~0.82
Mean	0.78	0.78	0.77
Median	0.78	0.78	0.76
<b>Length to depth ratio</b>			
Range	0.11~6.06	0.11~6.06	0.30~2.56
Mean	0.84	0.87	0.87
Median	0.77	0.77	0.72

320



321 **4.2 Spatial distribution patterns**

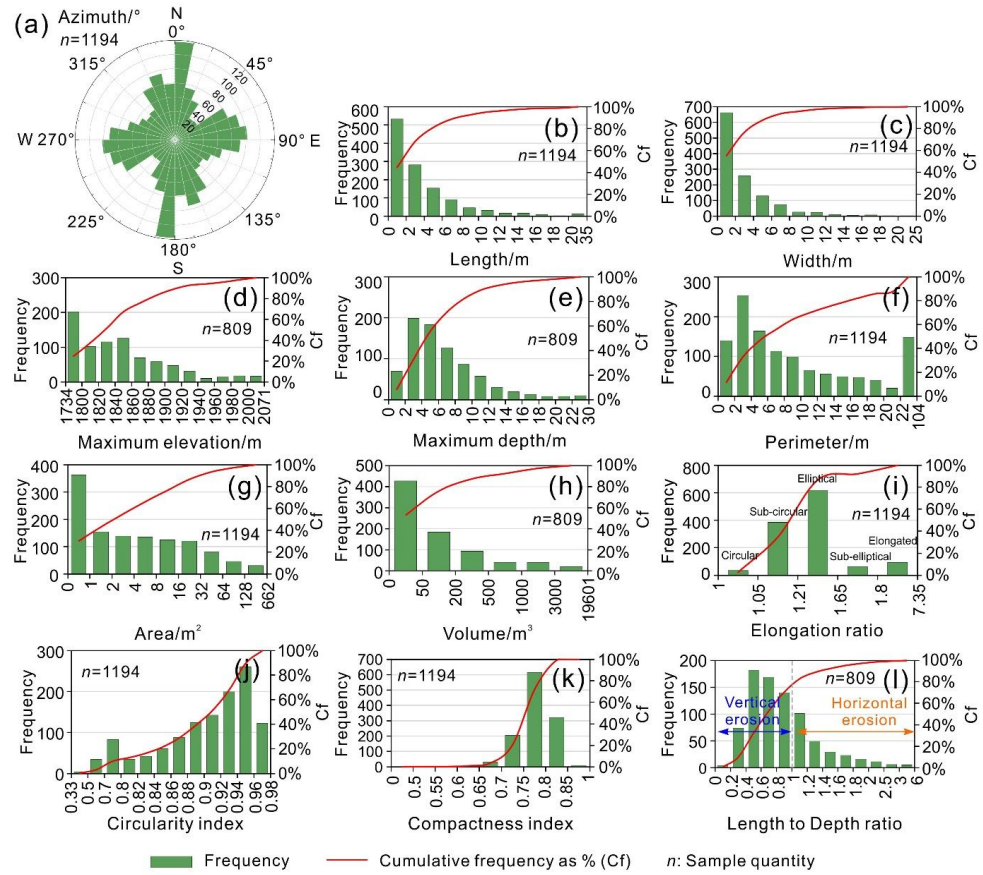
322 The spatial distribution patterns of the loess sinkholes have been analyzed considering  
323 their relationships with other geomorphic features (Fig. 3) and using spatial analysis and  
324 statistics tools (Fig. 8). The detailed geomorphological map of the Sunjiacha basin reveal that  
325 sinkholes are preferentially distributed in the following zones (Fig. 3): (1) the margins of the  
326 deeply entrenched lower-middle section of the Sunjiacha trunk stream; (2) tributary gully  
327 systems in the lower-middle part of the Sunjiacha basin; (3) landslides (slid mass and crown),  
328 mostly associated with the trunk channel; and (4) man-made terraces. The Kernel density model  
329 in Figure 8a shows low densities mainly associated with upper part of the Sunjiacha basin,  
330 where the drainage network shows lower degree of incision, and rounded divides characterized  
331 by low local gradients. Overall, there is a good spatial correlation between sinkholes and areas  
332 with high local topographic gradients and loess deposits disturbed by landslides. The hot spot  
333 model based on sinkhole area shown in Figure 8b illustrates a pronounced cluster of small  
334 sinkholes (cold spots in blue) associated with recent landslides in the lower sector of the basin.  
335 Clustering of large sinkholes (hot spots in red) mainly occur along the main drainages of  
336 tributary catchments in the lower part of the Sunjiacha basin.



337  
338 **Figure 8.** Spatial patterns of loess sinkholes: (a) Type and kernel density map (search radius:  
339 100 m); (b) Hot spot map by sinkhole area (threshold distance: 100 m).

340 **4.3 Morphometric analysis**

341 Here below we analyze the spatial and morphometric parameters computed for the 1194  
342 inventoried sinkholes (1162 single, 32 compound), their frequency-size distribution (Fig. 9), as  
343 well as some spatial patterns based on the distribution of different value ranges (Fig. 10).



344

345

**Figure 9.** Frequency distribution, represented as number of sinkholes and cumulative

346

frequency in percentage, of different spatial and morphometric parameters of the inventoried

347

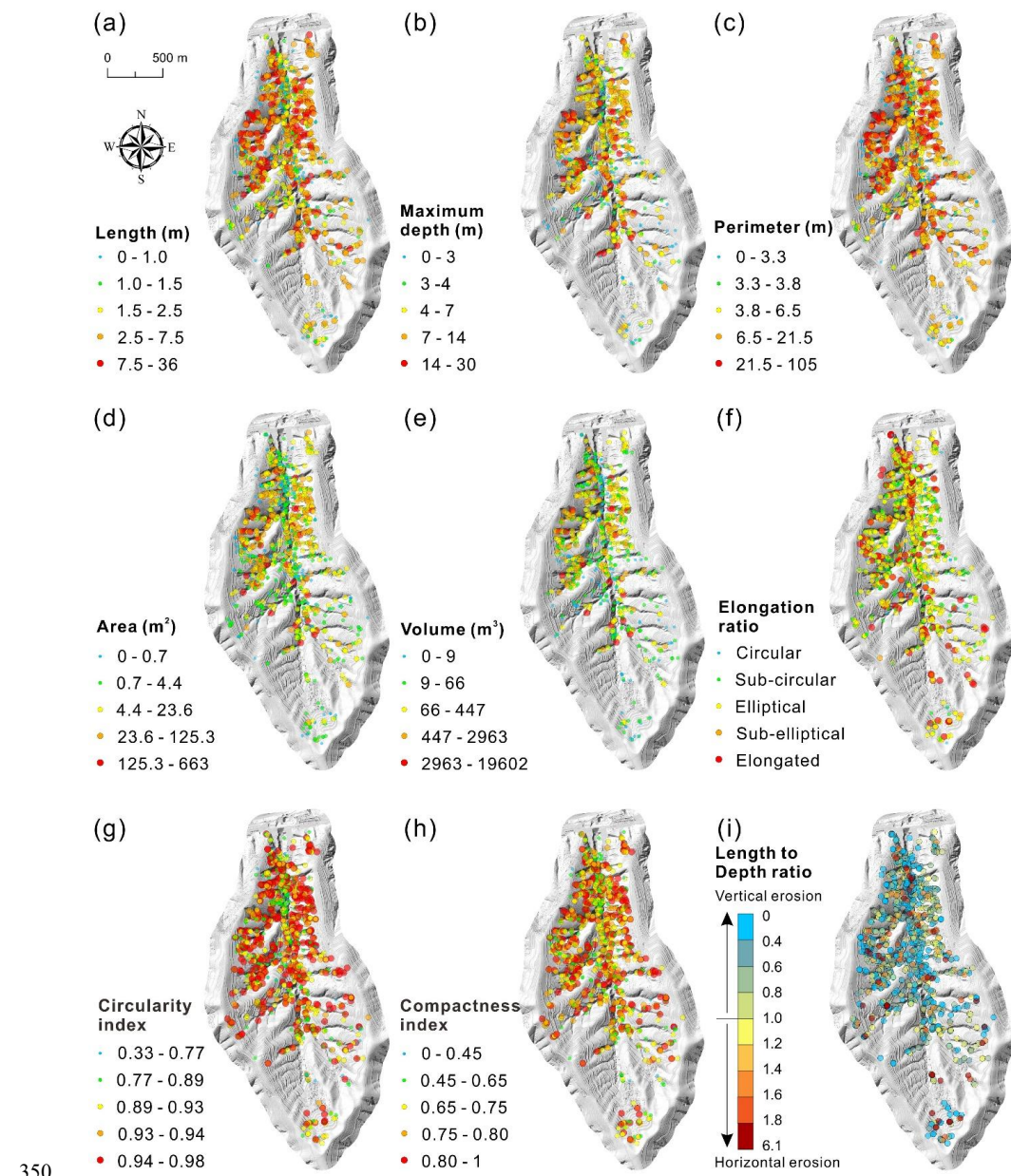
sinkholes: (a) Azimuth; (b) Length; (c) Width; (d) Maximum elevation; (e) Maximum depth;

348

(f) Perimeter; (g) Area; (h) Volume; (i) Elongation ratio; (j) Circularity index; (k)

349

Compactness index; (l) Length to Depth ratio.



350  
351 **Figure 10.** Spatial distribution of the sinkholes categorized into five value ranges: (a) Length;  
352 (b) Maximum depth; (c) Perimeter; (d) Area; (e) Volume; (f) Elongation ratio; (g) Circularity  
353 index; (h) Compactness index; (i) Length to Depth ratio.



354     *4.3.1 Spatial parameters*

355     The analyzed spatial parameters include the orientation of the sinkholes (azimuth) and the  
356     maximum elevation. The rose diagram in [Figure 9a](#) illustrates the frequency distribution of the  
357     azimuth of the major axes of sinkholes, showing preferred N-S and W-E orientations. The  
358     number of sinkholes in the Sunjiacha basin decreases as elevation increases ([Fig. 9d](#)). In the  
359     relatively low elevation range of 1734~1860 m, there are 545 sinkholes (67.37%), while the  
360     number of sinkholes in the relatively mid-elevation range of 1860~1960 m, and in the high-  
361     elevation range of 1960~2071 m are 216 (26.58%), and 48 (6.05%), respectively.  
362     Approximately 94% of the sinkholes are located in the more dissected mid and low elevation  
363     areas, despite they represent 76% of the basin area.

364     *4.3.2 Planimetric morphometric parameters*

365     The analyzed planimetric morphometric parameters include length, width, perimeter, area,  
366     elongation ratio, circularity index, and compactness index. The frequency distribution of the  
367     length ([Fig. 9b](#)) and width ([Fig. 9c](#)) of sinkholes exhibits a consistent pattern, characterized by  
368     exponential decay as the values increase. The number of sinkholes with lengths and widths  
369     ranging from 0 to 2 m is the highest, totaling 533 (44.64%) and 661 (55.36%), respectively.  
370     Conversely, sinkholes exceeding 10 m in length and width account for only 7.45% and 4.19%  
371     of the total sample, respectively. The map in [Figure 10a](#) reveals that sinkhole length shows some  
372     spatial patterns, with smaller sinkholes preferentially occurring in areas with lower degree of  
373     dissection (i.e., head of the basin and slopes close to the basin divides) and in recent landslides  
374     associated with the trunk stream.



375        Regarding the ratio between length and width (elongation ratio, *ER*), [Basso et al. \(2013\)](#)

376        and [Zumpano et al. \(2019\)](#) classified the plan shape of sinkholes into five categories: circular  
377        ( $ER \leq 1.05$ ), sub-circular ( $1.05 < ER \leq 1.21$ ), elliptical ( $1.21 < ER \leq 1.65$ ), sub-elliptical  
378        ( $1.65 < ER \leq 1.8$ ), elongated ( $ER > 1.8$ ). [Figures 9i](#) and [10f](#) show that sinkholes tend to have some  
379        degree of elongation, but without showing any clear spatial pattern in relation to this parameter.

380        Elliptical shapes dominate in the study area, with 618 sinkholes (51.76%), followed by sub-  
381        circular morphologies with 384 depressions (32.16%). Elongated sinkholes also represent a  
382        considerable number, totaling 93 (7.79%). Circular and sub-elliptical sinkholes are relatively  
383        infrequent, with 35 (2.93%) and 64 (5.36%), respectively. Similarly to length and width, the  
384        frequency of sinkhole perimeter and area shows a general decreasing trend as the size increases  
385        ([Figs. 9f, g](#)). The maximum perimeter and area reach 104 m and 662 m<sup>2</sup>, respectively. Sinkholes  
386        with a perimeter  $\leq 4$  m represent 21.9% (253) of the inventory, and 30.40% those with an area  
387         $\leq 1$  m<sup>2</sup>. In agreement with length and width, sinkholes with large perimeter and area tend to  
388        occur in sectors of the basin where the drainage net shows a greater degree of entrenchment,  
389        with the exception of some recent landslides ([Figs. 8b, 10c, and 10d](#)).

390        The circularity index (*CLI*) quantitatively assesses how much the shape of a sinkhole  
391        deviates from a perfect circle. *CLI* is equal to 1 in the case of a perfect circular shape and attains  
392        progressively lower values as it becomes less circular (e.g., elongated, irregular edge). The  
393        circularity index statistics indicate that 89.87% (1073 sinkholes), 60.64% (724 sinkholes), and  
394        10.30% (123 sinkholes) of the mapped sinkholes have a *CLI* greater than 0.8, 0.9, and 0.96,  
395        respectively ([Figs. 9j, 10g](#)). The compactness index (*COI*) also quantifies how close is the shape



396 of the sinkhole perimeter to a circle. The elongation and/or complexity of the sinkhole perimeter  
397 contributes to reduce the *COI* below 1. The loess sinkholes with a *COI* greater than 0.6, 0.7,  
398 and 0.8 represent 99.58% (1189 sinkholes), 96.40% (1151 sinkholes), and 27.72% (331  
399 sinkholes) of the sinkholes, respectively (Figs. 9k, 10h). The statistics of both the *CLI* and *COI*  
400 reveal that the perimeter of a great proportion of the sinkholes significantly deviates for a  
401 circular shape, in agreement with the calculated elongation ratios. Moreover, these parameters  
402 do not show any general cartographic pattern, with the exception of a high proportion of  
403 sinkholes with low *CLI* and *COI* values in some landslides associated with the trunk stream  
404 (Figs. 10g, h).

405 **4.3.3 3D morphometric parameters**

406 Three-dimensional parameters are those that incorporate the vertical dimension, including  
407 maximum depth, volume, and Length to Depth ratio. Note that large-area and large-perimeter  
408 sinkholes may have reduced volume if their depth is low. The frequency distribution of the  
409 maximum depth of the sinkholes in the study area shows a positively skewed distribution (Fig.  
410 9e). Sinkholes with depths ranging from 2 to 6 m represent 47.22% of the sample (382  
411 sinkholes). Only 58 sinkholes exceed a maximum depth of 14 m, representing just 7.17% of the  
412 total. The deepest sinkhole reaches an extraordinary value of 29.6 m and the average maximum  
413 depth is 6.55 m. The frequency of the sinkhole volume decreases exponentially as the size  
414 increases, with maximum and average values of 19,601 m<sup>3</sup> and 335 m<sup>3</sup>, respectively (Fig. 9h).  
415 A total of 428 sinkholes (52.90%) have volumes of  $\leq 50$  m<sup>3</sup>. The maps in Figures 10b and 10e  
416 show that deeper sinkholes and large-volume sinkholes ( $> 500$  m<sup>3</sup>) preferentially occur



417 associated with deeply incised gullies.

418 To some extent, the length and depth of the sinkholes reflect the horizontal and vertical  
419 development of the depressions, respectively. Thus, the Length to Depth ratio ( $LDr$ ) indicates  
420 whether sinkholes have greater horizontal ( $LDr > 1$ ) or vertical  $LDr < 1$ ) dimension. The relative  
421 value of these parameters can be influenced by multiple factors and processes, some favoring  
422 greater lengths (e.g., sinkhole expansion, sinkhole coalescence) and others greater depth (e.g.,  
423 deep subsurface conduits, erosion at the floor of sinkhole with bottom outlet). The frequency  
424 distribution of the  $LDr$  shows a positively skewed distribution, with 569 sinkholes (70.33%)  
425 having a  $LDr$  lower than 1 (greater depth than length), while those with a  $LDr$  greater than 1  
426 represent 29.67% (240) of the sinkholes with depth data (Fig. 9I). These values indicate that  
427 subsurface vertical erosion dominates in the formation of loess sinkholes in the study area,  
428 largely due to the development of relatively deep pipes within the thick loess cover (Fig. 10I).

429 **4.4 Frequency-size relationships**

430 The semi-log graph in Figure 11 represents separately the length of the 1162 single  
431 sinkholes and the 32 compound sinkholes mapped in the Sunjiacha basin, versus relative  
432 cumulative frequency. The latter indicates the frequency of sinkholes equal or larger than a  
433 given length. The length distribution of the single sinkholes, ranging from 35.1 m to 0.2 m and  
434 covering 2.3 orders of magnitude (i.e., log Max/Min), shows a wider range than the compound  
435 sinkholes, spanning 1.6 orders of magnitude from 33.9 m to 0.9 m. As expected, compound  
436 sinkholes tend to reach larger dimensions (i.e., plotted to the right), with a length value for the  
437 cumulative frequency of 0.5, 1.7 times larger than that of single sinkholes (3.8 m vs. and 2.2



438 m).

439 In both cases, the empirical cumulative frequency-size distribution can be modelled  
440 satisfactorily by logarithmic functions (natural logarithm) with a high goodness of fit ( $R^2 > 0.97$ ).  
441 The regression of the compound sinkholes describes adequately the distribution for the whole  
442 length range. In contrast, the empirical distribution of the single sinkholes deviates from the  
443 fitted curve for both small ( $< 0.4$  m) and large dimensions ( $> 12.7$  m). These cut-off or rollover  
444 points indicate lower empirical frequencies for the smaller sinkholes and higher empirical  
445 frequencies for the larger sinkholes than those shown by the regression. Given the completeness  
446 of the sinkhole inventory, the lower rollover can be attributed to physical constraints, such as  
447 the minimum span of a pipe-roof required for a collapse to occur. The upper rollover could be  
448 related to factors such as the expansion of single sinkholes and the depth distribution of  
449 sinkhole-forming underground pipes, which in the study area can reach significant depths given  
450 the high thickness of the loess cover. Note that sinkholes reach a maximum depth of 29.6 m.

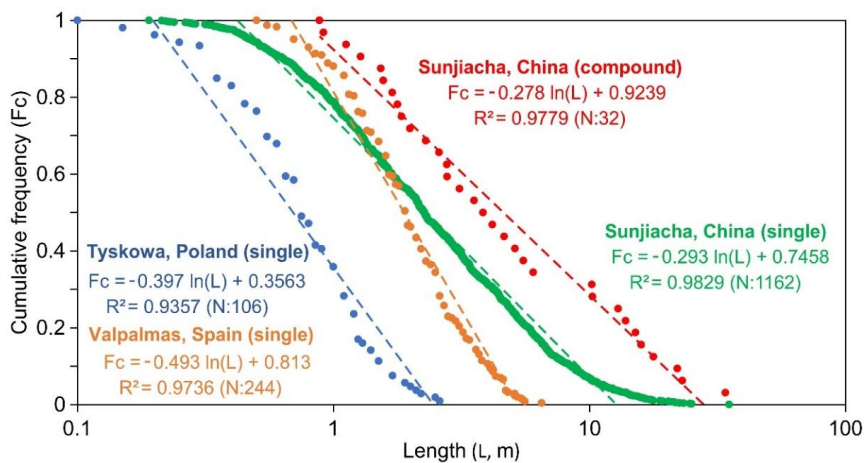


**Figure 11.** Graph showing the cumulative frequency-size distribution of single and compound sinkholes in the study area, as well as single piping sinkholes in other regions with different



454 soils and environmental conditions (Tyskowa, Bieszczady Mountains, Poland; Valpalmas,  
455 Ebro Basin, NE Spain).

## 456 4.5 Relationships between different parameters

457 The planimetric (length, width, perimeter, area) and three-dimensional (maximum depth,  
458 volume) size parameters of the sinkholes were fitted pairwise in a matrix diagram showing  
459 graphically and with regressions (power functions) the relationships between each pair of  
460 morphometric parameters (Fig. 12). As expected, the regressions of pairs of planimetric  
461 parameters have always high goodness of fit  $R^2 > 0.94$ . In contrast, the relationship between  
462 planimetric and 3D parameters is poorer.  $R^2$  is always  $< 0.6$  in the case of maximum depth, and  
463 lower than  $\leq 0.9$  in the case of volume.

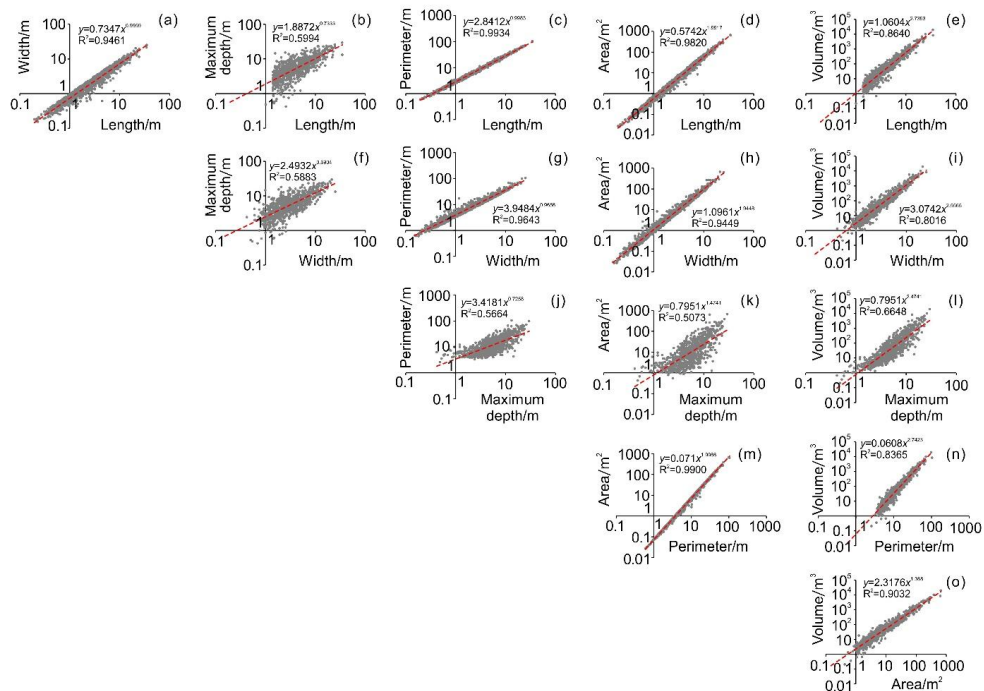


**Figure 12.** Matrix diagram showing pairwise fitting relationships of planimetric (length, width, perimeter, area) and 3D (maximum depth, volume) morphometric parameters.



467 **4.6 Subsurface soil erosion**

468 Sinkhole development, including cavity-roof collapse and expansion of sinkhole margins  
469 by mass wasting processes, can contribute significantly to soil erosion, despite it is largely  
470 overlooked worldwide. The complete and accurate sinkhole inventory constructed in the  
471 Sunjiacha basin, including volumetric data, provides an excellent opportunity to assess the  
472 impact of sinkhole-related soil erosion within the context of the Loess Plateau. We calculated  
473 the soil loss associated with each sinkhole by multiplying the volume of each depression by the  
474 soil's dry bulk density, as shown in Figure 13a. Figure 13b illustrates the frequency distribution  
475 of soil loss related to individual sinkholes: 0~1 t (389 sinkholes, 32.58%); 1~14 t (211 sinkholes,  
476 17.67%); 14~177 t (361 sinkholes, 30.23%); 177~2014 t (194 sinkholes, 16.25%); 2014~24973  
477 t (39 sinkholes, 3.27%). The aggregate volume of sinkholes ( $27.08 \times 10^4$  m<sup>3</sup>) multiplied by the  
478 soil's dry bulk density (1.27 t/m<sup>3</sup>) yields a total soil loss for the basin of  $34.50 \times 10^4$  t. Considering  
479 the area of the basin (2400 ha), the specific soil erosion related to sinkholes can be estimated at  
480 143.75 t/ha. Note that these values do not include hidden non-collapsed pipes. Figure 13a shows  
481 that the impact of the process is quite uneven, with a much greater contribution in the lower  
482 half of the basin and in the areas associated with deeply incised gullies.



(a)

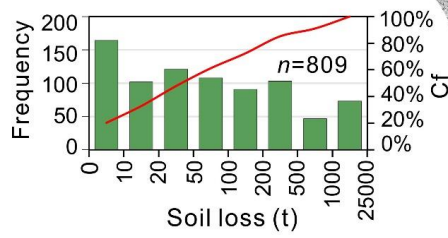
**Soil loss by sinkholes (t)**

- 0-1 (389 sinkholes)
- 1-14 (211 sinkholes)
- 14-177 (361 sinkholes)
- 177-2104 (194 sinkholes)
- 2104-24973 (39 sinkholes)

0 250 500 m



(b)



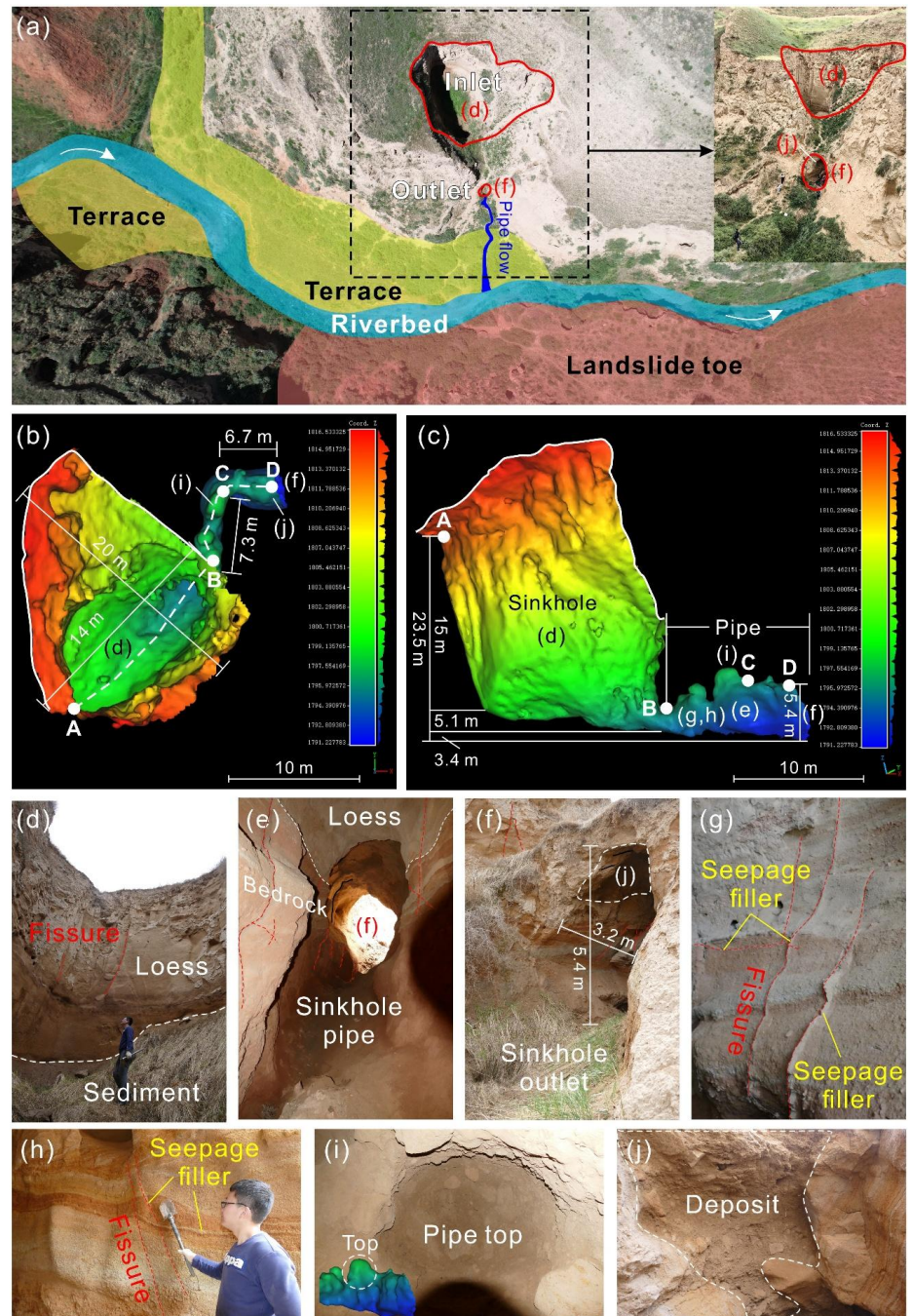
483

484 **Figure 13.** Soil loss by sinkholes. (a) Spatial distribution map indicating soil erosion related  
485 to individual sinkholes; (b) Frequency distribution histogram and cumulative frequency (Cf)  
486 curve of soil loss by individual sinkholes.



487 **4.7 In-depth investigation of a complex sinkhole**

488 Point clouds captured by airborne LiDAR surveys cover most of the sinkhole topography,  
489 thanks to the vertical orientation of the sensors. However, obtaining comprehensive point  
490 clouds of the interior of sinkholes proves challenging due to obstructions and complex  
491 morphology. To address the limitations of airborne LiDAR scanning, we employed a handheld  
492 laser scanner to conduct an in-depth investigation in the interior of thirteen representative  
493 sinkholes. [Figures 14a-j](#) shows the field photographs and 3D models of a loess sinkhole  
494 (HLS01). Morphometric measurements indicate that the perimeter of the sinkhole at the land  
495 surface is 49.7 m, with an area of 179.6 m<sup>2</sup> and a maximum vertical depth of 20.1 m. We adopted  
496 both the traditional method and the point cloud slicing algorithm to estimate the volume of this  
497 sinkhole. The results show a volume and soil loss of 3610 m<sup>3</sup> and 4585 t calculated by the  
498 former method, while the latter yielded values of 1750 m<sup>3</sup> and 2223 t, respectively ([Table 3](#)).  
499 Due to the fact that the sinkhole has an inclined top opening and a sloping bottom underlain by  
500 deposits ([Figs. 14a, d](#)), the volume calculated by the traditional method was twice higher than  
501 the actual volume. This also proves that handheld laser scanning can capture more accurately  
502 the whole geometry of the sinkhole, overcoming the technical shortcomings of airborne LiDAR.



503

504

**Figure 14.** Investigation of the interior of a representative sinkhole with an opening at the



505 bottom (see [Figs. 5a and f](#)): (a) Location, general field view, and landforms; (b) 3D model  
 506 generated from GeoSLAM point clouds, labelled with morphometric measurements; (c)  
 507 Model slice along the AD profile line, labelled with morphometric measurements; (d)  
 508 Photograph of the sinkhole bottom; (e) Photograph of the pipe; (f) Sinkhole outlet; (g-h)  
 509 Bedrock exposed in the sinkhole wall; (i) Photograph of the pipe top; (j) Poorly-sorted  
 510 deposits including angular loess clasts accumulated in the sinkhole floor by collapse and mass  
 511 wasting processes.

512 **Table 3** Comparison of volume and soil loss calculated by traditional method and point cloud  
 513 slicing algorithm.

	Traditional method	Point cloud slicing algorithm
Data source	Airborne LiDAR	GeoSLAM LiDAR
Visualization		
	Vertical scanning by the UAS LiDAR	Multidirectional scanning by the handheld laser scanner.
Volume calculation principle	Volume= Area×Maximum depth ( <a href="#">Gökkaya et al., 2021</a> ; <a href="#">De Waele and Gutiérrez, 2022</a> )	The convex hull algorithm is used to slice the point clouds at a thickness of 0.2 m. The volume of each slice is calculated and then summed up to obtain the total volume.
Soil loss (SL)	$SL=\rho\times V$ , where $\rho$ is the dry density of soil, $V$ is the volume of the sinkhole.	
Results	V: 3610 m <sup>3</sup> SL: 4585 t	V: 1750 m <sup>3</sup> (shaft 1606 m <sup>3</sup> , pipe 144 m <sup>3</sup> ) SL: 2223 t



514        Interestingly, most sinkholes examined in the field display dominant vertical development,  
515        while this particular sinkhole exhibits a complex three-dimensional morphology comprising a  
516        vertical shaft connected to a subhorizontal pipe. The upper shaft-like portion of the sinkhole  
517        (20 m length  $\times$  14 m width  $\times$  20.1 m depth) is situated in loess deposits, while the lower portion  
518        (14 m length  $\times$  3.2 m width  $\times$  5.4 m height) is a gently inclined ellipsoidal conduit carved into  
519        horizontally bedded and jointed reddish sandstone. This lower conduit ends at the sinkhole  
520        outlet perched 8 m above the valley floor (Fig. 14a). We interpret that the development of this  
521        complex sinkhole started as a backward propagating conduit at the foot of the slope, associated  
522        with a seepage outlet point controlled by joints in the loess cover and the bedrock (Figs. 14d-  
523        h). Eventually, the enlarging conduit reached a sufficiently large span to initiate upward roof  
524        collapse, ultimately originating the sinkhole. At present, five distinct ceiling cupolas can be  
525        clearly observed at the top of this pipe (Figs. 14b, c and i), indicating sites of upward roof  
526        propagation (stoping). The incision of the drainage network within a context of rapid crustal  
527        uplift resulted in the sinkhole outlet being hanged 8 m above the current thalweg.

528        Additionally, we observed a significant accumulation of horizontally stratified flood  
529        deposits resting atop the aeolian loess on the fluvial strath terrace (Fig. 14a). The interior of the  
530        sinkhole is relatively cool and damp, with the bottom underlain by collapsed soil. We found  
531        remnants of past flash-flood or debris-flow deposits on the sinkhole floor, as well as on the  
532        walls and outlet ceiling of the connected lateral pipe (Figs. 14d, f, j). These sediments may  
533        include: (1) Horizontally bedded deposits accumulated during floods in the drainage, with a  
534        stage high enough to cause the penetration of flood waters into the sinkhole outlet



535 (backflooding); (2) Massive to poorly stratified deposits derived from collapse and mass  
536 wasting processes acting primarily in the pipe roof and sinkholes margins, respectively.

## 537 **5 Discussion**

### 538 **5.1 Contributions of different factors to the sinkhole development**

539 The development of loess sinkholes is influenced by multiple factors of different nature,  
540 such as topography, climate, hydrology, soil texture, joints and fissures, animal activity, plant  
541 root systems, human activity (Bernatek-Jakiel and Poesen, 2018; Peng et al., 2018; Geng et al.,  
542 2021; Hu et al., 2022; Kariminejad et al., 2023; Li et al., 2024). At the scale of a small basin,  
543 climate exhibits minimal variation. We focus our analysis on the relationships between loess  
544 sinkholes and variables related to catchment topography, geomorphology, hydrology, and land  
545 use. In order to better understand the controlling factors, a number of topographic and  
546 geomorphic indices and variables, such as Slope, Total Catchment Area (TCA), Topographic  
547 Wetness Index (TWI), Valley Depth (VD), Channel Network Distance (CND), Landslides, and  
548 Landuse, were computed with the open-source SAGA GIS platform and subsequently mapped  
549 in ArcMap 10.5 (Figs. 15a-g). The selection of these indices and variables is primarily based  
550 on the following considerations: (1) Slope provides the inherent hydraulic gradient conditions  
551 for rainfall infiltration and surface runoff concentration, controlling the piping process leading  
552 to sinkhole development; (2) Total Catchment Area is the upslope land surface that contributes  
553 surface and near-surface flow to a given outlet, pixel, or stream segment (Gallant and  
554 Hutchinson, 2011). It is a proxy for the potential volume of water that can reach a pipe or a  
555 sinkhole site, having influence on their initial formation and subsequent morphological



556 evolution; (3) Topographic Wetness Index is a steady-state, terrain-based proxy for soil  
557 moisture and surface saturation potential. It quantifies the tendency of water to accumulate at  
558 any location by integrating local slope with the upslope contributing area (Moore et al., 1991);  
559 (4) Valley Depth is a measure of the vertical distance from a valley's highest ridges down to its  
560 lowest points. It is a proxy of the degree of dissection; (5) Channel Network Distance represents  
561 the vertical height from a location to the nearest stream. Its value on valley margins depends on  
562 both gradient and planimetric distance to the nearest drainage; (6) Landslides can remodel the  
563 local topography and significantly disturb loess deposits, reducing their mechanical strength  
564 and increasing their permeability, which in turn favor piping and sinkhole development; (7)  
565 Landuse mainly reflects the impact of human activity, notably terracing, on piping and sinkhole  
566 development.

567 In order to assess the spatial relationships between sinkholes and the different indices and  
568 variables, we calculated normalized frequencies for different intervals. This normalized  
569 frequency ( $F_n$ ) is given by the ratio between the proportion of sinkholes in the interval and the  
570 proportion of the area of that interval. The higher the value of this 'likelihood ratio', the higher  
571 the spatial concurrence between sinkholes and the areas with values within the interval (Figs.  
572 15a1-g1). These data, together with the findings presented in the results contribute to shed light  
573 into the formation and spatial distribution of the loess sinkholes.

574 Overall, the normalized frequency graphs show that the distribution of sinkholes is  
575 primarily controlled by hydrological, topographic and geomorphic factors. Water availability is  
576 an essential factor, in as much as subsurface flow is the geomorphic agent responsible for piping



577 development. This is illustrated by the higher normalized frequencies of sinkholes in areas with  
578 high Total Catchment Area ( $>100 \text{ m}^2$ ;  $F_n=2.97$ ) and high Topographic Wetness Index ( $>9$ ;  
579  $F_n=4.92$ ). Slope is the main governing topographic factor, which largely determines hydraulic  
580 gradient and the erosional capability of subsurface flow. Sinkholes preferentially occur in high  
581 gradient areas and close to incised gullies, with high Slope ( $>40^\circ$ ;  $F_n=1.82$ ), high Valley Depth  
582 ( $>10 \text{ m}$ ;  $F_n=1.98$ ), low Channel Network Distance ( $<1 \text{ m}$ ;  $F_n=1.98$ ), and areas primarily  
583 classified as erosional gullies ( $F_n=2.53$ ). A good spatial correlation is also observed between  
584 sinkholes and landslides, with a normalized frequency of sinkholes within landslides ( $F_n=3.42$ ).  
585 These spatial patterns are clearly recognizable in the detailed geomorphological map (Fig. 3)  
586 and the Kernel density (Fig. 8a) and hot spot maps (Fig. 8b). The latter shows that sinkholes  
587 developed on landslides tend to be smaller. This could be attributed to a younger age of those  
588 sinkholes, developed on a more recent geomorphic surface.

589 The vast majority of the sinkholes occur in erosional gullies (71.44%, 853 sinkholes). This  
590 pattern is consistent with findings reported for soil pipes in other regions worldwide (Verachtert  
591 et al., 2010; Kariminejad et al., 2023). Incised gullies may foster the development of pipes and  
592 sinkholes through various mechanisms (Bernatek-Jakiel and Poesen, 2018; Peng et al., 2018):  
593 (1) create steep hydraulic gradients; (2) guide converging surface and subsurface drainage; (3)  
594 favor the development of inlet points (e.g., unloading cracks) and outlet points for seepage flow.  
595 As shown in Figures 6c-f, rows of sinkholes occur along the bottom of erosional gullies. These  
596 sinkholes can be connected through groundwater seepage channels, as confirmed by electrical  
597 resistivity tomography surveys in previous studies (Hu et al., 2022). It can be anticipated that,



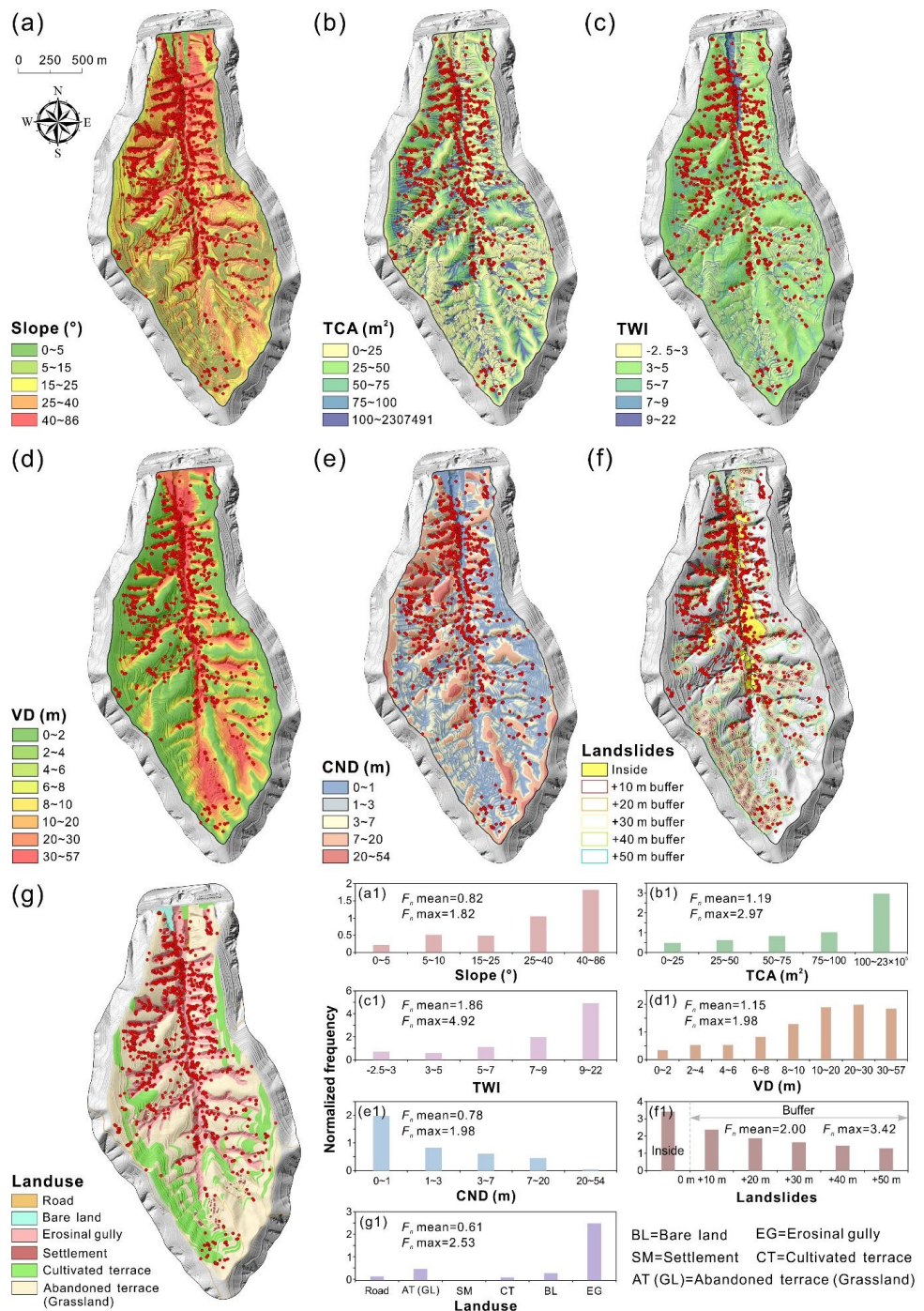
598 with the expansion and coalescence of the sinkholes, the gully will experience significant  
599 entrenchment and will turn into a drainage dominated by surface flow.

600 Another interesting feature is the close association between landslides and sinkholes in the  
601 Sunjiacha basin. Previous studies have shown that soil pipes in slopes favor efficient drainage  
602 and, to some extent, help maintain slope stability (Pierson, 1983; Uchida et al., 2001; Sidle and  
603 Bogaard, 2016). However, the sinkholes mapped on the landslides have mostly formed after the  
604 development of the slope movements. The greater susceptibility of landslide ground to piping  
605 and sinkhole development can be attributed to several factors: (1) landsliding contributes to  
606 weaken the loess deposits; (2) the internal deformation of the landslide mass typically involves  
607 a bulking effect (dilation and volume expansion) accompanied by a permeability increase; and  
608 (3) fissures and other pathways for focused water infiltration are common on landslides (Hu et  
609 al., 2020, 2022). At some sites, a causal relationship between landslides and sinkholes can be  
610 inferred, showing a cascading geomorphic effect. Figures 15f and f1 illustrate that landslides  
611 play an important role in the development of sinkholes. The distance to landslides seems to  
612 control the development of sinkholes, but this control effect gradually decays with increasing  
613 distance from the landslide boundary. Statistics show that as many as 251 sinkholes (accounting  
614 for 21%) have developed within the landslides, making the landslide interior the second largest  
615 contributor to sinkhole formation ( $F_n=3.42$ ). Approximately 43% of sinkholes are distributed  
616 within the landslide and its outward 20m buffer zone ( $F_n=1.87$ ). The size of the sinkholes (e.g.,  
617 length, area and volume), which can be considered as a proxy for their age, seems to be  
618 influenced by the age of the geomorphic surface. Mature sinkholes tend to be larger due to



619 expansion and coalescence, and they usually occur on old geomorphic surfaces (such as old  
620 gullies, river terraces and ancient landslides). Conversely, sinkholes developed on landslides  
621 that have occurred in the past few years or decades tend to be smaller. This pattern is clearly  
622 depicted in the hot spot map shown in [Figure 8b](#).

623 In recent decades, due to a significant decrease in the local agricultural population and the  
624 implementation of policies that promote the conversion of farmland back to forests and  
625 grasslands, approximately 74% of the terraced fields have been abandoned for cultivation. The  
626 landuse map ([Figs. 15g, g1](#)) shows that abandoned terraces have evolved into grasslands in the  
627 Sunjiacha basin. Abandoned terraces (25.63%, 306 sinkholes) appear to be more prone to  
628 sinkhole formation than cultivated terraces (2.51%, 30 sinkholes). This can be related to more  
629 favorable conditions in the abandoned terraces and the lower preservation potential of the  
630 sinkholes in the cultivated terraces, where sinkholes tend to be filled soon after their formation.  
631 Without a doubt, pipe collapses and gully development pose threats to land productivity,  
632 agricultural sustainability, soil nutrient levels, and the carbon cycle, while also potentially  
633 destabilizing socio-economic conditions ([Llena et al., 2024](#)). By contrast, roads, bare land, and  
634 settlement sites seem to exert almost no influence on sinkhole occurrence.





636 **Figure 15.** Spatial relationships between sinkholes and different indices and variables  
637 expressed as maps (a-g) and normalized frequency graphs. (a1-g1).

638 5.2 Spatial and morphological features

639 Sinkholes tend to be elongated and preferentially oriented in the Sunjiacha basin (Figs. 9a,  
640 i). The majority of the major axes of the sinkholes align closely with the directions of the trunk  
641 (N-S) and secondary (E-W) channels in the watershed (Fig. 3). These directions tend to guide:  
642 (1) subsurface water flow and the trend of pipes generated by internal erosion, and (2) the  
643 orientation of unloading cracks (e.g., scarped channel margins) through which water can  
644 infiltrate. Both the pipes and the cracks influence the horizontal development of the sinkholes  
645 by mass wasting processes acting in the margins and coalescence (e.g., merging of aligned  
646 sinkholes connected to a common pipe).

647 The altitudinal distribution of sinkholes (Fig. 9d) may be governed by several factors: (1)  
648 the density and entrenchment degree of the drainage network is higher at lower elevations; (2)  
649 ground disturbed by landslides chiefly occurs at low elevation areas associated with the trunk  
650 Sunjiacha stream; (3) high-elevation zones (e.g., rounded drainage divides) generally have  
651 lower topographic gradient, lower degree of dissection, thinner loess cover, and more restricted  
652 runoff contributing areas.

653 The deeper and larger sinkholes tend to be distributed in the deeper valleys (Figs. 10b, e).  
654 This pattern can be attributed to the development of deeper subsurface pipes in areas with  
655 thicker loess, greater topographic gradient and lower local base level. Thicker loess tends to  
656 accumulate in paleotopographic lows, which subsequently guide gully networks.

657 The goodness of fit between the planimetric and 3D parameters of the sinkholes is



658 relatively poor (Fig. 12). This indicates a limited dependence between the horizontal and  
659 vertical dimensions of sinkholes, in agreement with the wide range shown by the Length to  
660 Depth ratio (0~6). That is, sinkholes with small area can have significant depth and volume,  
661 and sinkholes with limited volume can reach relatively large areas. This is also reflected by the  
662 relatively poor fit shown between the two 3D parameters (volume and maximum depth;  
663  $R^2=0.66$ ). Even so, the fitting equations presented in Figure 12 provide preliminary empirical  
664 support for characterizing and predicting scaling relationships for sinkholes in the Loess Plateau.

665 **5.3 Frequency-size relationships of sinkholes in different soils and environments**

666 The cumulative frequency-size graph in Figure 11 shows that the length distribution of the  
667 compound sinkholes (red) is clearly displaced towards larger dimensions with respect to the  
668 single sinkholes (green). The average length of the compound and single sinkholes are 7.37 m  
669 and 3.65 m, respectively. This expected deviation in the size distribution can be explained by  
670 the different sets of processes that operate in the development of the two sinkhole populations.  
671 The size of the single sinkholes is related to pipe-roof collapse and the subsequent expansion  
672 of the scarped edge of the depressions by erosional processes, mainly mass wasting and gullyling.  
673 The size tends to increase with the time elapsed since the initial collapse, as the sinkhole edge  
674 recedes. Compound sinkholes result from the coalescence of adjoining and expanding sinkholes  
675 and/or the occurrence of a new sinkhole intersecting a pre-existing one, leading to the sudden  
676 enlargement of the depressions. The contribution of these processes (coalescence, intersection)  
677 is influenced by the density and clustering degree of the sinkholes, in as much as the likelihood  
678 of sinkhole aggregation is greater in tightly clustered sinkhole populations (Bernatek-Jakiel et



679 al., 2019; De Waele and Gutiérrez, 2022; Sevil and Gutiérrez, 2023). Moreover, sinkhole  
680 merging entails a decrease in sinkhole density by number and a substantial increase in sinkhole  
681 size.

682 Figure 11 shows the cumulative frequency-length distribution of the single and compound  
683 sinkholes mapped in the Sunjacha basin, together with the single sinkholes inventoried in two  
684 catchments with contrasting geological and climatic conditions (Bernatek-Jakiel et al., 2019):  
685 Valpalmas in the Ebro Cenozoic Basin (NE Spain), and Tyskowa in the Bieszczady Mountains  
686 of the Outer Eastern Carpathians (Poland). The pipe collapses in Valpalmas occur in Holocene  
687 valley-fill alluvium consisting of indurated and Na-rich cohesive clayey silt that reaches around  
688 8 m in thickness. Here, the climate is semiarid (mean precipitation 500 mm) and sinkholes tend  
689 to occur associated with the edge of erosional scarps, showing a tightly clustered distribution.

690 The pipe collapses in the Tyskowa catchment can be considered as a representative sample of  
691 those inventoried in several catchments of the Bieszczady Mts., characterized by a humid  
692 climate (mean precipitation 900 m; Bernatek-Jakiel et al., 2019). Here, sinkholes occur on  
693 relatively thin slope deposits with some eolian component consisting of poorly indurated clayey  
694 silt. The single sinkholes in Valpalmas (orange) show a similar size to the single sinkholes in  
695 Sunjacha for the central cumulative frequencies (i.e.,  $F_c$  0.5~0.6). Nonetheless, single  
696 sinkholes in Valpalmas display a much narrower length range (1.1. vs. 2.3 orders of magnitude,  
697 steeper curve) and significantly smaller maximum dimensions (6.5 m vs 35.1 m). The more  
698 restricted size range of the small sinkholes can be attributed to the fact that the inventory in  
699 Valpalmas was restricted to sinkholes with lengths  $\geq 0.5$  m. The differences between



700 Sunjachá and Valpalmas can be ascribed to factors such as the greater morpho-sedimentary  
701 diversity of Sunjachá, where sinkholes occur in a broad range of deposits and geomorphic  
702 settings (e.g., loess, colluvium, alluvium), and the wide depth range of sinkhole-forming pipes,  
703 substantiated by the measured maximum depth of the sinkholes, ranging from 29.6 to 0.42 m  
704 (Figs. 9e, 10b and 14c). Single sinkholes in the humid Biezsyczady Mts. of Poland are much  
705 smaller, mainly because they occur on thinner and mechanically weaker deposits. The weaker  
706 the soils, the smaller the largest span that can reach cavities before collapse. Induration of the  
707 deposits by secondary carbonate (i.e., cementation) in this humid environment is less significant  
708 than in the semiarid environments of Valpamas and the Loess Plateau.

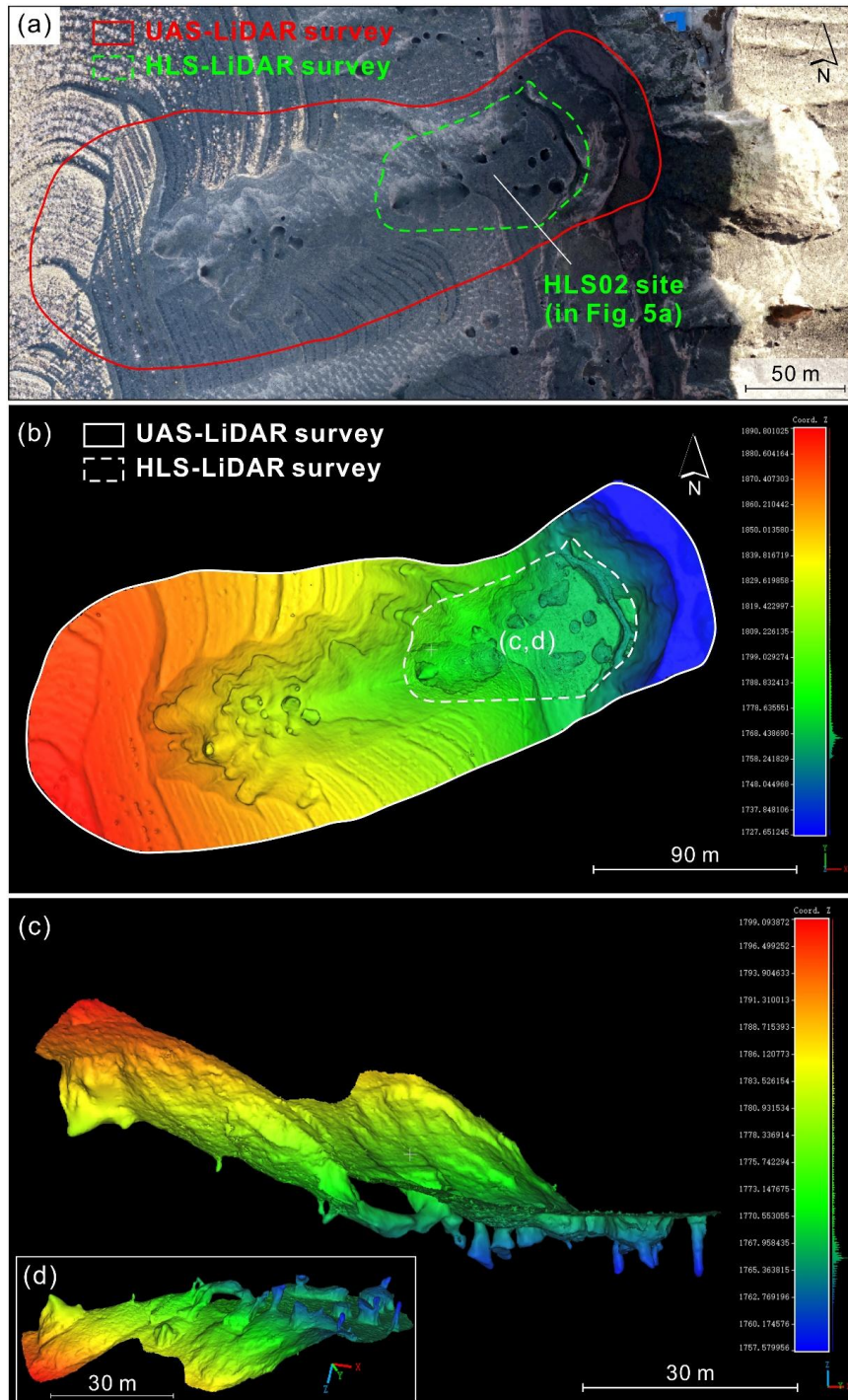
709 **5.4 Limitations and prospects**

710 Extensive field surveys reveal that loess sinkholes possess highly complex three-  
711 dimensional morphologies, rather than a simple cylindrical or conical shape (Figs. 6i, 7c, 14b  
712 and 16; Hu et al., 2024). This is illustrated by the high-resolution scanning of 142 sinkholes  
713 with a handheld laser device carried out in 2021 in a small basin, named Laozigou, east of our  
714 study area (Hu et al., 2024; Jiang et al., 2024). The data can be accessed at  
715 <https://doi.org/10.1016/j.geomorph.2024.109404>. As shown in Table 3, volume estimates based  
716 on airborne LiDAR point clouds and simplified volume estimation methods can lead to highly  
717 inaccurate approximations. The aggregate volume, and hence the inferred soil loss reported in  
718 our study area may therefore be overestimated. Several factors may contribute to the deviation  
719 between the actual volume and the volume calculated, leading to over- or under-estimations: (1)  
720 volumes are calculated using maximum depth and assuming a cylindrical geometry, but



721 sinkholes may be conical (overestimation) or the actual depth may be deeper (underestimation);  
722 (2) sinkholes may be connected to conduits that cannot be imaged in airborne surveys, resulting  
723 in underestimations.

724 Encouragingly, the comprehensive point clouds acquired by the handheld scanner enable  
725 us to develop far more precise cloud-slicing and volumetric-integration algorithms for exact  
726 volume computation (Hu et al., 2024). This will enable us to develop a more reliable fitting  
727 formula relating sinkhole area and volume, which could be used for refining the results obtained  
728 from the UAS surveys. We conducted a survey of a gully by jointly employing UAS-LiDAR  
729 and HLS--LiDAR technologies and found that the integrated point cloud data can effectively  
730 delineate the internal structure and connectivity of sinkholes, as they overcome the limitations  
731 of a single LiDAR technology. Meanwhile, machine-learning approaches for the automatic  
732 detection and delineation of sinkholes are rapidly emerging and showing promising results (Zhu  
733 et al., 2016, 2020; Jiang et al., 2024; Li et al., 2024; Coşkuner et al., 2025; Creati et al., 2025).  
734 Indeed, we have already implemented an end-to-end workflow that couples airborne LiDAR  
735 point clouds with deep-learning models to achieve automatic sinkhole identification, instance  
736 segmentation, feature extraction, cataloguing, and mapping (Li et al., 2025, in press).





738     **Figure 16.** Sinkhole investigations by jointly using UAS-LiDAR and HLS-LiDAR: (a) The  
739     survey areas of the two LiDAR devices; (b) The mesh model generated from the merged point  
740     cloud data; (c) The side view of mesh model of HLS-LiDAR survey area; (d) The bottom  
741     view of c.

742     **6 Data availability**

743     The dataset supporting this study is openly available on Zenodo at  
744     <https://doi.org/10.5281/zenodo.14000267> (Hu et al., 2025).

745     **7 Conclusions**

746     High-resolution models derived from photographs and LiDAR data captured with a UAS  
747     have allowed the production of a comprehensive cartographic inventory of loess sinkholes in a  
748     catchment ( $2,4 \text{ km}^2$ ) of the Chinese Loess Plateau with a high density of sinkholes (ca. 500  
749     sinkholes/ $\text{km}^2$ ). The spatial data, including a bare-surface digital surface model and a 3D terrain  
750     point cloud, was appropriate for accurately mapping the sinkholes, differentiating between  
751     single (1194) and compound depressions (288), and extracting precise planimetric  
752     morphometric parameters. This is the first morphometric dataset available for the piping-related  
753     sinkholes of the Chinese Loess Plateau. Three dimensional parameters such as depth and  
754     volume can be also extracted or estimated, although with much higher uncertainty. Rough  
755     cumulative volume estimates yield sinkhole-related soil erosion values of around 140 t/ha. The  
756     work illustrates that the limitations of the airborne data for measuring 3D morphometric  
757     parameters can be overcome by using SLAM-based handheld scanners. The 3D point clouds  
758     obtained with these devices at specific sinkholes, although labor intensive, allow measuring  
759     precisely the volume of the scanned voids. Nonetheless, hidden pipes, which may account for



760 a significant volume of subsurface erosion, remain elusive for these direct surveying techniques.

761 The sinkholes in the analyzed catchment tend to be elongated (52% with elongation ratio

762 1.21-1.65) and preferentially oriented following the dominant trends of the drainage network.

763 They show a broad range of dimensions, ranging from 0.19 to 35.11 m in length (2.3 orders of

764 magnitude). As expected, compound sinkholes tend to be significantly larger than single

765 sinkholes (7.37 m versus 3.65 m in average length, respectively), although the degree of

766 coalescence is rather moderate (single 97.3%; compound 2.7%). A remarkable feature of the

767 investigated sinkholes is their large vertical dimension. Around 70% of the sinkholes are deeper

768 than longer. The average and maximum depths are 6.5 m and 29.6 m, respectively, indicating

769 the development of deep-seated pipes in thick loess cover or even within the jointed and friable

770 sandstone bedrock. Comparison with other morphometric datasets from semiarid Spain (fine

771 grained alluvium) and humid Poland (thin loess-rich colluvium) reinforces the large size of the

772 studied sinkholes in the Chinese loess, developed on much thicker loess and generally rooted

773 in deeper pipes. The frequency-size relationships produced could be transformed in sinkhole

774 hazard curves incorporating the time dimension (i.e., timing of sinkhole occurrence).

775 The spatial relationships between the sinkholes and other geomorphic features and various

776 topographic and hydrologic indices reveal that their development is mainly controlled by the

777 amount of water available for subsurface flow (i.e., runoff contributing area) and topographic

778 gradient. Sinkhole preferentially occur associated with the steep margins of deeply incised

779 streams and gully networks. Recent landslides, underlain by weakened and more porous

780 disturbed loess deposits are also identified as areas especially prone to piping and sinkhole



781 occurrence.

782 **Author contributions.**

783 SH, FG, FZ, and SL designed the study and wrote the manuscript. SH, FG, and SL  
784 compiled and analyzed the dataset. SH, XW, JS, and SW performed field investigation. NW,  
785 XL, and FG supervised and reviewed the manuscript. All authors contributed to the writing and  
786 editing of this paper.

787 **Competing interests.**

788 The contact author has declared that neither they nor their co-authors have any competing  
789 interests.

790 **Disclaimer.**

791 Publisher's note: Copernicus Publications remains neutral with regard to jurisdictional  
792 claims in published maps and institutional affiliations

793 **Acknowledgements.**

794 The authors are grateful to Dr. Anita Bernatek-Jakiel for providing published  
795 morphometric data on piping sinkholes in the Valpalmas (Spain) and the Tyskowa (Poland)  
796 catchments. The work by FG has been supported by the project DIAPERNO (PID2021-  
797 123189NB-I00) of the Spanish Government (Ministerio de Ciencia e Innovación). FG belongs  
798 to the IUCA and the Geoenvironmental Processes and Global Change (E02\_23R) research  
799 group financed by the Aragón Government and the European Social Fund (ESF-FSE).

800 **Financial support.**

801 This research has been supported by the National Natural Science Foundation of China



802 (grant nos. 42371009, 42001006 and 42230712), the National Key Research and Development  
803 Program of China (grant nos. 2022YFC3003401 and 2023YFC3008401).

804

805

806 **References**

807 Basso, A., Bruno, E., Parise, M., and Pepe, M.: Morphometric analysis of sinkholes in a karst  
808 coastal area of southern Apulia (Italy), *Environ. Earth Sci.*, 70, 2545–2559, 2013.

809 Bernatek, A.: The Influence of Piping on Mid-Mountain Relief: A Case Study from the Polish  
810 Bieszczady Mts. (Eastern Carpathians), *Carpath J Earth Env.*, 10, 107–120, 2015.

811 Bernatek-Jakiel, A., Jakiel, M., and Krzemień, K.: Piping dynamics in mid-altitude mountains  
812 under a temperate climate: Bieszczady Mountains, eastern Carpathians, *Earth Surf Proc  
813 Land*, 42, 1419–1433, 10.1002/esp.4160, 2017.

814 Bernatek-Jakiel, A. and Kondracka, M.: Combining geomorphological mapping and near  
815 surface geophysics (GPR and ERT) to study piping systems, *Geomorphology*, 274, 193–  
816 209, 2016.

817 Bernatek-Jakiel, A. and Poesen, J.: Subsurface erosion by soil piping: significance and research  
818 needs, *Earth-Sci Rev.*, 185, 1107–1128, 10.1016/j.earscirev.2018.08.006, 2018.

819 Bernatek-Jakiel, A., Gutiérrez, F., Nadal-Romero, E., and Jakiel, M.: Exploring the frequency-  
820 size relationships of pipe collapses in different morphoclimatic regions, *Geomorphology*,  
821 345, 106845, 10.1016/j.geomorph.2019.106845, 2019.

822 Borah, U. K., Gond, A., Rajan, P. P., Sivan, R., and Vivekanandan, N.: Joint geomorphological  
823 and geophysical (electrical resistivity) investigation for the configuration of soil pipe,  
824 *Contrib Geophys Geod.*, 52, 239–255, 10.31577/congeo.2022.52.2.4, 2022.

825 Brlmo, E., Calcaterra, D., and Parise, M.: Development and morphometry of sinkholes in  
826 coastal plains of Apulia, southern Italy. Preliminary sinkhole susceptibility assessment,  
827 *Eng Geol.*, 99, 198–209, 10.1016/j.enggeo.2007.11.017, 2008.

828 Cole, J. P.: Study of major and minor civil divisions in political geography, The 20th



829 international geographical congress, London, 1964.

830 Coskuner, B., İnce, İ., and Barstuğan, M.: Sinkhole detection via deep learning using DEM  
831 images, *Nat Hazards*, 121, 8347–8366, 10.1007/s11069-025-07127-0, 2025.

832 Creati, N., Paganini, P., Sterzai, P., and Pavan, A.: Mapping of karst sinkholes from LIDAR  
833 data using machine-learning methods in the Trieste area, *J Spat Sci*, 70, 365–380,  
834 10.1080/14498596.2025.2469176, 2025.

835 Day, M.: Doline morphology and development in Barbados, *Annals of the Association of*  
836 *American Geographers*, 73, 206–219, 1983.

837 De Carvalho Júnio, O. A., Guimarães, R. F., Montgomery, D. R., Gillespie, A. R., Gomes, R.  
838 A. T., De Souza Martins, É. D., and Silva, N. C.: Karst Depression Detection Using  
839 ASTER, ALOS/PRISM and SRTM-Derived Digital Elevation Models in the Bambu  
840 Group, Brazil, *Remote Sens*, 6, 330–351, 10.3390/rs6010330, 2014.

841 De Waele, J. and Gutiérrez, F.: Karst hydrogeology, geomorphology and caves, John Wiley &  
842 Sons, 888 p, 2022.

843 Donnelly, L. J.: Subsidence and associated ground movements on the Pennines, northern  
844 England, *Q J Eng Geol Hydroge*, 41, 315–332, Doi 10.1144/1470-9236/07-216, 2008.

845 Farrant, A. R. and Cooper, A. H.: Karst geohazards in the UK: the use of digital data for hazard  
846 management, *Q J Eng Geol Hydroge*, 41, 339–356, Doi 10.1144/1470-9236/07-201, 2008.

847 Gallant, J. C. and Hutchinson, M. F.: A differential equation for specific catchment area, *Water*  
848 *Resour Res*, 47, W05535, 10.1029/2009wr008540, 2011.

849 Gao, Y., Alexander, E. J. R., and Barnes, R. J.: Karst database implementation in Minnesota:  
850 analysis of sinkhole distribution, *Environ Geol*, 47, 1083–1098, 10.1007/s00254-005-  
851 1241-2, 2005.

852 Gao, Y., Alexander, E.C., Tipping, R.: The development of a karst feature database for  
853 southeastern Minnesota. *J. Cave Karst Stud.* 64, 51–57, 2002.

854 Geng, H. P., Liu, R., Zheng, W. S., Zhang, Y. B., Xie, R., Guo, Y., and Pan, B. T.: Interaction  
855 Between Animal Burrowing and Loess Cave Formation in the Chinese Loess Plateau,  
856 *Front Earth Sci*, 9, 806921, 10.3389/feart.2021.806921, 2021.



857 Geng, H. P., Xu, W. Y., Zheng, W. S., Gao, X. L., and Pan, B. T.: A hybrid mechanism for the  
858 initiation and expansion of loess caves across the Chinese Loess Plateau, *Land Degrad  
859 Dev*, 34, 3329–3339, 10.1002/ldr.4686, 2023.

860 Gibbs, H.S.: Tunnel-gully erosion on the Wither Hills, Marlborough. *New Zealand Journal of  
861 Science and Technology* 27(A2), 135–146, 1945.

862 Gökkaya, E., Gutiérrez, F., Ferk, M., and Görüm, T.: Sinkhole development in the Sivas gypsum  
863 karst, Turkey, *Geomorphology*, 386, 107746, 10.1016/j.geomorph.2021.107746, 2021.

864 Gutiérrez, F., Desir, G., and Gutiérrez, M.: Causes of the catastrophic failure of an earth dam  
865 built on gypsiferous alluvium and dispersive clays (Altorricon, Huesca Province, NE  
866 Spain), *Environ Geol*, 43, 842–851, 10.1007/s00254-002-0700-2, 2003.

867 Gutiérrez, F., Parise, M., De Waele, J., and Jourde, H.: A review on natural and human-induced  
868 geohazards and impacts in karst, *Earth-Sci Rev*, 138, 61–88,  
869 10.1016/j.earscirev.2014.08.002, 2014.

870 Hofierka, J., Gallay, M., Bandura, P., and Šašák, J.: Identification of karst sinkholes in a forested  
871 karst landscape using airborne laser scanning data and water flow analysis,  
872 *Geomorphology*, 308, 265–277, 10.1016/j.geomorph.2018.02.004, 2018.

873 Hu, S., Gutiérrez, F., Zhang, F., Li, S., Wang, N., Li, X., and Wang, X.: A morphological dataset  
874 of loess sinkholes from a small basin in the Chinese Loess Plateau (1.0) [Data set]. Zenodo.  
875 <https://doi.org/10.5281/zenodo.14000267>, 2025.

876 Hu, S., Jiang, Z.D., Wang, N.L., Zhang, F.Y., Chen, Y.X., Wu, S.B., Wang, L., Li, S.S.: In Situ  
877 Dataset of Loess Sinkholes using UAS and LiDAR Technology in Huining County, China  
878 (2024). Digital Journal of Global Change Data Repository,  
879 <https://doi.org/10.3974/geodb.2024.05.05.V1>, 2024.

880 Hu, S., Qiu, H. J., Wang, N. L., Cui, Y. F., Wang, J. D., Wang, X. G., Ma, S. Y., Yang, D. D.,  
881 and Cao, M. M.: The influence of loess cave development upon landslides and  
882 geomorphologic evolution: A case study from the northwest Loess Plateau, China,  
883 *Geomorphology*, 359, 107167, 10.1016/j.geomorph.2020.107167, 2020.

884 Hu, S., Qiu, H. J., Wang, N. L., Wang, X. G., Ma, S. Y., Yang, D. D., Wei, N., Liu, Z. J., Shen,



885 Y. D., Cao, M. M., and Song, Z. P.: Movement process, geomorphological changes, and  
886 influencing factors of a reactivated loess landslide on the right bank of the middle of the  
887 Yellow River, China, *Landslides*, 19, 1265–1295, 10.1007/s10346-022-01856-0, 2022.

888 Jiang, Z. D., Hu, S., Deng, H., Wang, N. L., Zhang, F. Y., Wang, L., Wu, S. B., Wang, X. A.,  
889 Cao, Z. W., Chen, Y. X., and Li, S. S.: Detection and automatic identification of loess  
890 sinkholes from the perspective of LiDAR point clouds and deep learning algorithm,  
891 *Geomorphology*, 465, 109404, 10.1016/j.geomorph.2024.109404, 2024.

892 Jones, E. and Beck, D.: The use of three-dimensional laser scanning for deformation monitoring  
893 in underground mines, *Proceedings of the 13th AusIMM Underground Operators  
894 Conference*: 66, 267–270, 2017.

895 Kariminejad, N., Sepehr, A., Poesen, J., and Hassanli, A.: Combining UAV remote sensing and  
896 pedological analyses to better understand soil piping erosion, *Geoderma*, 429, 116267,  
897 10.1016/j.geoderma.2022.116267, 2023.

898 Kim, C. E. and Anderson, T. A.: Digital disks and a digital compactness measure, *Proceedings  
899 of the sixteenth annual ACM symposium on Theory of computing*, ACM Press, New York,  
900 117–124, 1984.

901 Kobal, M., Bertoncelj, I., Pirotti, F., Dakskobler, I., and Kutnar, L.: Using Lidar Data to Analyse  
902 Sinkhole Characteristics Relevant for Understory Vegetation under Forest Cover-Case  
903 Study of a High Karst Area in the Dinaric Mountains, *Plos One*, 10, e0122070,  
904 10.1371/journal.pone.0122070, 2015.

905 Konsolaki, A., Vassilakis, E., Gouliotis, L., Kontostavlos, G., and Giannopoulos, V.: High  
906 Resolution Digital 3d Modelling of Subsurface Morphological Structures of Koutouki  
907 Cave, Greece, *Acta Carsologica*, 49, 163–177, 10.3986/ac.v49i2-3.7708, 2020.

908 Lee, E. J., Shin, S. Y., Ko, B. C., and Chang, C.: Early sinkhole detection using a drone-based  
909 thermal camera and image processing, *Infrared Phys Techn*, 78, 223–232,  
910 10.1016/j.infrared.2016.08.009, 2016.

911 Li, S., Hu, S., Wang, L., Sun, J., Zhang, F., Wang, N., Wang, X., Wu, S., Xu, Z., and Pang, G.:  
912 LSPNet: Automatic Identification and Segmentation of Loess Sinkholes in 3D Point



913       Clouds Using an Enhanced PointNet++, Available at SSRN 5414065,  
914       <https://papers.ssrn.com/sol3/Delivery.cfm?abstractid=5414065>, 2025

915       Li, S. S., Hu, S., Wang, L., Zhang, F. Y., Wang, N. L., Wu, S. B., Wang, X. A., and Jiang, Z. D.:  
916       Quantifying the Geomorphological Susceptibility of the Piping Erosion in Loess Using  
917       LiDAR-Derived DEM and Machine Learning Methods, *Remote Sens.*, 16, 4203,  
918       10.3390/rs16224203, 2024.

919       Li, W. W., Goodchild, M. F., and Church, R.: An efficient measure of compactness for two-  
920       dimensional shapes and its application in regionalization problems, *Int J Geogr Inf Sci*, 27,  
921       1227–1250, 10.1080/13658816.2012.752093, 2013.

922       Li, X., Song, Y., and Ye, W.: Engineering geological research on tunnel-erosion in loess, *Tongji*  
923       University Press, Shanghai, 2010. (in Chinese)

924       Li, X. A., Wang, L., Hong, B., Li, L. C., Liu, J., and Lei, H. N.: Erosion characteristics of loess  
925       tunnels on the Loess Plateau: A field investigation and experimental study, *Earth Surf Proc*  
926       Land, 45, 1945–1958, 10.1002/esp.4857, 2020.

927       Llena, M., Carreras, S., Bernatek-Jakiel, A., Ollero, A., and Nadal-Romero, E.: Agricultural  
928       land abandonment linked to pipe collapse and gully development: Reconstruction from  
929       archival SfM and LiDAR datasets, *Geoderma*, 449, 116995,  
930       <https://doi.org/10.1016/j.geoderma.2024.116995>, 2024.

931       Liu, H. X. and Wang, L.: Mapping detention basins and deriving their spatial attributes from  
932       airborne LiDAR data for hydrological applications, *Hydrol Process*, 22, 2358–2369,  
933       10.1002/hyp.6834, 2008.

934       Liu, T.S.: Loess Deposits in the Middle Reaches of the Yellow River, Science Press, Beijing,  
935       1–234, 1964. (in Chinese)

936       Liu, T.S.: Loess Deposits in China, Science Press, Beijing, 1–244, 1965. (in Chinese)

937       Panno, S. V. and Luman, D. E.: Mapping palimpsest karst features on the Illinois sinkhole plain  
938       using historical aerial photography, *Carbonate Evaporite*, 28, 201–214, 10.1007/s13146-  
939       012-0107-4, 2013.

940       Mokroš, M., Mikita, T., Singh, A., Tomaštík, J., Chudá, J., Węzyk, P., Kuželka, K., Surový, P.,



941 Klimánek, M., Zieba-Kulawik, K., Bobrowski, R., and Liang, X. L.: Novel low-cost  
942 mobile mapping systems for forest inventories as terrestrial laser scanning alternatives, *Int*  
943 *J Appl Earth Obs*, 104, 102512, 10.1016/j.jag.2021.102512, 2021.

944 Moore, I. D., Grayson, R., and Ladson, A.: Digital terrain modelling: a review of hydrological,  
945 geomorphological, and biological applications, *Hydrol Process*, 5, 3–30, 1991.

946 Morgan, R. P. C.: *Soil erosion and conservation*, 3rd edition, Blackwell Publishing, the United  
947 Kingdom, 2005.

948 Niu, Y. N.: Study on provenance of Quaternary loess in Longxi area: a case from Huining,  
949 Lanzhou University Thesis, 2023. (in Chinese)

950 Öztürk, M. Z., Şener, M. F., Şener, M., and Şimşek, M.: Structural controls on distribution of  
951 dolines on Mount Anamas (Taurus Mountains, Turkey), *Geomorphology*, 317, 107–116,  
952 10.1016/j.geomorph.2018.05.023, 2018.

953 Panno, S., Weibel, C. P., and Li, W.: Karst regions of Illinois, Open file series 1997-02,  
954 <http://hdl.handle.net/10111/UIUCOCA:karstregionsofil19972pann>, 1997.

955 Peng, J. B., Sun, P., Igwe, O., and Li, X.: Loess caves, a special kind of geo-hazard on loess  
956 plateau, northwestern China, *Eng Geol*, 236, 79–88, 10.1016/j.enggeo.2017.08.012, 2018.

957 Peng, S.S.: Pronounced changes in atmospheric circulation and dust source areas during the  
958 mid-Pleistocene implicated by the Huining loess-soil sequence from the northeastern  
959 margin of the Tibetan Plateau, China University of Geosciences (Beijing) PhD Thesis,  
960 2014. (in Chinese)

961 Pierson, T. C.: Soil pipes and slope stability, *Q. J. Eng. Geol. Hydrogeol.*, 16, 1-11, 1983.

962 Poesen, J.: Soil erosion in the Anthropocene: Research needs, *Earth Surf Proc Land*, 43, 64–84,  
963 10.1002/esp.4250, 2018.

964 Rajabi, A.: Sinkhole Detection and Quantification Using LiDAR Data. Electronic Theses and  
965 Dissertations, 5776. <https://stars.library.ucf.edu/etd/5776>, 2018.

966 Richards, K. S. and Reddy, K. R.: Critical appraisal of piping phenomena in earth dams, *B Eng*  
967 *Geol Environ*, 66, 381–402, 10.1007/s10064-007-0095-0, 2007.

968 Sevil, J. and Gutiérrez, F.: Morphometry and evolution of sinkholes on the western shore of the



969 Dead Sea. Implications for susceptibility assessment, *Geomorphology*, 434, 108732,  
970 10.1016/j.geomorph.2023.108732, 2023.

971 Sidle, R. C. and Bogaard, T. A.: Dynamic earth system and ecological controls of rainfall-  
972 initiated landslides, *Earth-Sci Rev*, 159, 275–291, 10.1016/j.earscirev.2016.05.013, 2016.

973 Uchida, T., Kosugi, K., and Mizuyama, T.: Effects of pipeflow on hydrological process and its  
974 relation to landslide: a review of pipeflow studies in forested headwater catchments,  
975 *Hydrol Process*, 15, 2151–2174, DOI 10.1002/hyp.281, 2001.

976 Vajedian, S. and Motagh, M.: Extracting sinkhole features from time-series of TerraSAR-  
977 X/TanDEM-X data, *ISPRS-J Photogramm Remote Sens*, 150, 274–284,  
978 10.1016/j.isprsjprs.2019.02.016, 2019.

979 Vennari, C. and Parise, M.: A Chronological Database about Natural and Anthropogenic  
980 Sinkholes in Italy, *Geosciences*, 12, 200, 10.3390/geosciences12050200, 2022.

981 Verachtert, E., Van den Eeckhaut, M., Poesen, J., and Deckers, J.: Factors controlling the spatial  
982 distribution of soil piping erosion on loess-derived soils: A case study from central  
983 Belgium, *Geomorphology*, 118, 339–348, 10.1016/j.geomorph.2010.02.001, 2010.

984 Wang, X. G., Hu, S., Lian, B. Q., Wang, J. D., Zhan, H. B., Wang, D. Z., Liu, K., Luo, L., and  
985 Gu, C. Y.: Formation mechanism of a disaster chain in Loess Plateau: A case study of the  
986 Pucheng County disaster chain on August 10, 2023, in Shaanxi Province, China, *Eng Geol*,  
987 331, 107463, 10.1016/j.enggeo.2024.107463, 2024.

988 Wu, Q. S., Deng, C. B., and Chen, Z. Q.: Automated delineation of karst sinkholes from LiDAR-  
989 derived digital elevation models, *Geomorphology*, 266, 1–10,  
990 10.1016/j.geomorph.2016.05.006, 2016.

991 Yang, S. and Ding, Z.: Spatial changes in grain size of loess deposits in the Chinese Loess  
992 Plateau and implications for palaeoenvironment, *Quaternary Sciences*, 37, 934–944, 2017.  
993 (in Chinese)

994 Yuan, Z. L., Ban, X. J., Han, F. Y., Zhang, X. Q., Yin, S. H., and Wang, Y. M.: Integrated three-  
995 dimensional visualization and soft-sensing system for underground paste backfilling, *Tunn  
996 Undergr Sp Tech*, 127, 104578, 10.1016/j.tust.2022.104578, 2022.



997 Zhang, W. M., Qi, J. B., Wan, P., Wang, H. T., Xie, D. H., Wang, X. Y., and Yan, G. J.: An Easy-  
998 to-Use Airborne LiDAR Data Filtering Method Based on Cloth Simulation, *Remote Sens.*,  
999 8, 501, 10.3390/rs8060501, 2016.

1000 Zhu, J. F., Nolte, A. M., Jacobs, N., and Ye, M.: Using machine learning to identify karst  
1001 sinkholes from LiDAR-derived topographic depressions in the Bluegrass Region of  
1002 Kentucky, *J Hydrol.*, 588, 125049, 10.1016/j.jhydrol.2020.125049, 2020.

1003 Zhu, J. F. and Pierskalla, W. P.: Applying a weighted random forests method to extract karst  
1004 sinkholes from LiDAR data, *J Hydrol.*, 533, 343–352, 10.1016/j.jhydrol.2015.12.012, 2016.

1005 Zumpano, V., Pisano, L., and Parise, M.: An integrated framework to identify and analyze karst  
1006 sinkholes, *Geomorphology*, 332, 213–225, 10.1016/j.geomorph.2019.02.013, 2019.